Climatology of the SKYHI Troposphere–Stratosphere–Mesosphere General Circulation Model

KEVIN HAMILTON, R. JOHN WILSON, J. D. MAHLMAN, AND L. J. UMSCHEID

Geophysical Fluid Dynamics Laboratory/NOAA, Princeton University, Princeton, New Jersey

(Manuscript received 2 December 1993, in final form 13 May 1994)

ABSTRACT

The long-term mean climatology obtained from integrations conducted with different resolutions of the GFDL "SKYHI" finite-difference general circulation model is examined. A number of improvements that have been made recently in the model are also described. The versions considered have 3° × 3.6°, 2° × 2.4°, and 1° × 1.2° latitude–longitude resolution, and in each case the model is run with 40 levels from the ground to 0.0096 mb. The integrations all employ a fixed climatological cycle of sea surface temperature. Over 25 years of integration with the 3° model and shorter integrations with the higher-resolution versions are analyzed. Attention is focused on the December–February and June–August periods.

The model does a reasonable job of representing the atmospheric flow in the troposphere and lower stratosphere. The simulated tropospheric climatology has an interesting sensitivity to horizontal resolution. In common with several spectral GCMs that have been examined earlier, the surface zonal-mean westerlies in the SKYHI extratropics become stronger with increasing horizontal resolution. However, this "zonalization" of the flow with resolution is not as prominent in the upper troposphere of SKYHI as it is in some spectral models. It is noteworthy that—without parameterized gravity wave drag—the SKYHI model at all three resolutions can simulate a realistic separation of the subtropical and polar night jet streams and a fairly realistic strength of the lower-stratospheric winter polar vortex.

The geographical distribution of the annual-mean and seasonal precipitation are reasonably well simulated. When compared against observations in an objective manner, the SKYHI global precipitation simulation is found to be as good or better than that obtained by other state-of-the-art general circulation models. However, some significant shortcomings remain, most notably in the summer extratropical land areas and in the tropical summer monsoon regions. The time-mean precipitation simulation is remarkably insensitive to the horizontal model resolution employed. The other tropospheric feature examined in detail is the tropopause temperature. The whole troposphere suffers from a cold bias of the order of a few degrees Celcius, but in the 3° SKYHI model this grows to about 6°C at 100 mb. Interestingly, the upper-tropospheric bias is reduced with increasing horizontal resolution, despite that the cloud parameters in the radiation code are specified identically in each version.

The simulated polar vortex in the Northern Hemisphere winter in the upper stratosphere is unrealistically confined to high latitudes, although the maximum zonal-mean zonal wind is close to observed values. Near the stratopause the June–August mean temperatures at the South Pole are colder than observations by ~65°C, 50°C, and 30°C in the 3°, 2°, and 1° simulations, respectively. The corresponding zonal-mean zonal wind patterns display an unrealistically strong polar vortex. The extratropical stratospheric stationary wave field in the Northern Hemisphere winter is examined in some detail using the multiyear averages available from the 3° SKYHI integration. Comparison with comparable long-term mean observations suggests that the model captures the amplitude and phase of the stationary waves rather well.

The SKYHI model simulates the reversed equator–pole temperature gradient near the summer mesopause. The simulated summer polar mesopause temperatures decrease with increasing horizontal resolution, although even at 1° resolution the predicted temperatures are still warmer than observed. The increasing resolution is accompanied by increased westerly driving of the mean flow in the summer mesosphere by dissipating gravity waves. The present results suggest that the SKYHI model does explicitly resolve a significant component of the gravity waves required to produce the observed summer mesopause structure.

The semiannual oscillation near the tropical stratopause is reasonably well simulated in the 3° version. The main deficiency is in the westerly phase, which is not as strong as observed. There is also a second peak in the amplitude of the semiannual wind oscillation at the top model level (0.0096 mb) corresponding to the observed mesopause semiannual oscillation. This simulated mesopause oscillation is weaker (by a factor of ~3) than that observed. The simulation in the tropical stratopause and mesosphere changes quite significantly with increasing resolution, however. In the tropical lower stratosphere of the 3° model the zonal-mean zonal wind displays a very weak (~3 m s^{-1} peak to peak) interannual variation, which—while rather irregular—does display a roughly biennial period and the downward phase propagation that is characteristic of the observed quasi-biennial oscillation.

Corresponding author address: Dr. Kevin Hamilton, GFDL/NOAA, Princeton University, P.O. Box 308, Princeton, NJ 08542.

1. Introduction

A fundamental goal of meteorological research over the last four decades has been the construction of comprehensive numerical models that can faithfully reproduce the observed general circulation of the global atmosphere. While much progress has been made in general circulation model (GCM) studies, some rather basic questions remain. The problems begin even in tropospheric GCMs that employ realistic prescribed ocean surface temperatures. Given the strong vertical thermal coupling in the troposphere, the first-order simulation of thermal structure is reasonably well assured. However, it turns out to be difficult to simulate even a basic quantity like the surface wind field (or meridional gradient in surface pressure). In particular, it has been found for many models that surface westerlies in the midlatitudes increase markedly with the horizontal resolution employed (Manabe et al. 1979; Boer and Lazare 1988). At sufficiently high resolution the results become quite unrealistic. The intensification of westerly flow with increasing resolution also afflicts the simulation of the upper troposphere of some GCMs.

Simulation of the middle atmospheric circulation from first principles is inherently an even harder problem, given the lack of direct coupling with prescribed surface conditions. Thus, it is not surprising that GCMs have often failed to capture even some of the first-order features of the wind and temperature structure of the middle atmosphere. In particular, comprehensive model simulations of the thermal structure in the extratropical middle atmosphere have generally been unrealistically close to radiative equilibrium. Thus, the simulated winter polar vortex is often too cold and the simulated summer polar mesopause is unrealistically warm. The severity of these problems differs from model to model and can vary depending on horizontal resolution. The cold winter pole problem is also generally much more severe in the Southern Hemisphere (SH) than in the Northern Hemisphere (NH). Another important deficiency in current GCMs is their apparent inability to simulate anything approximating a realistic quasi-biennial oscillation (QBO).

Of course, some of the deficiencies noted above can be reduced by the addition of some parameterization of the momentum fluxes due to subgrid-scale topographic or traveling gravity waves (e.g., Palmer et al. 1986; McFarlane 1987; Rind et al. 1988a; Rind et al. 1988b). Unfortunately, it is difficult to demonstrate (even very roughly) the quantitative validity of any particular parameterization that might be used. Parameterizations of the full spectrum of the traveling gravity wave field are extremely arbitrary (Lindzen 1981; Holton 1982; Rind et al. 1988a). Even the intrinsically simpler problem of computing the momentum flux convergence associated with subgrid-scale topographic waves is subject to great uncertainties in both the overall magnitude of the effect expected and its vertical distribution. The simple approach adopted by McFarlane and others is to assume that the vertical momentum flux is constant up to a breaking level predicted by WKB theory. In midlatitudes this breaking level is generally above the jet stream core, and this leads to a significant drag on the upper-troposphere and lower-stratosphere mean westerlies. Imposition of such a drag can have rather dramatic effects on the simulation of both the tropospheric westerlies and the stratospheric winter vortex (Laursen and Eliasen 1989; Boville 1991). However, Broccoli and Manabe (1992) find improved results in the troposphere can be obtained by arbitrarily modifying the simple WKB parameterization to spread out the momentum flux divergence uniformly from the ground to the predicted breaking level. Numerical experiments have shown that gravity waves forced by small-scale orography may indeed break at quite low levels in the troposphere (e.g., Peltier and Clark 1979).

In light of all these uncertainties, there remains the possibility that the subgrid-scale drag parameterization imposed may simply compensate for some other deficiency in the simulation. Thus, for example, gravity wave drag in the troposphere of a particular model may help reduce overly intense mean surface westerlies, which are actually related to unrealistically strong meridional eddy momentum fluxes (e.g., Klinker and Sardeshmukh 1992). The fact that the need for subgrid-scale gravity wave drag is generally found to increase with improved model resolution suggests that the modeling difficulties may be of a more fundamental nature.

This discussion forms the background for the present paper, which documents the performance of the 40-level Geophysical Fluid Dynamics Laboratory (GFDL) "SKYHI" troposphere–stratosphere–mesosphere finite-difference GCM. Over the last 15 years different versions of this model have been featured in a number of published studies of middle atmospheric phenomena (Fels et al. 1980; Mahlman and Sinclair 1980; Andrews et al. 1983; Mahlman and Umscheid 1984, 1987; Hayashi et al. 1984, 1989; Miyahara et al. 1986; Hamilton and Mahlman 1988; Hamilton 1989, 1993a,b, 1994a,b; Manzini and Hamilton 1993; Strahan and Mahlman 1994a,b; Mahlman et al. 1994). Up to this point, however, the basic model climatology has not been extensively documented. The present paper will summarize the SKYHI model design with an emphasis on recent improvements and then will consider the results for the long-term mean climatology obtained in control simulations at three different horizontal resolutions. The consideration of model performance as a function of horizontal resolution makes this paper similar to such earlier works as Manabe et al. (1979), Boer and Lazare (1988), Boville (1991), and Boyle (1993). It turns out that the behavior of the SKYHI model (in both the troposphere and the middle atmosphere) differs in some interesting ways from that of the spectral models discussed in these earlier papers. The present paper in-

cludes consideration of two particularly ambitious integrations that are unprecedented for a comprehensive GCM with a serious representation of the middle atmosphere: one integration (with moderate horizontal resolution) extending for more than 25 years, and one (of two-year duration) run at very high (1° × 1.2°) horizontal resolution. A wide variety of both tropospheric and middle atmospheric fields from these integrations will be examined (and compared with observations). Attention will be focused almost exclusively on the solstitial seasons December–February (DJF) and June–August (JJA). All the simulations discussed here were run without any parameterization of subgrid-scale gravity wave effects.

This paper is organized as follows. Section 2 describes the model formulation and the details of the various control integrations to be analyzed. Section 3 discusses the observational climatological datasets that are used to compare with various aspects of the model simulations. Section 4 looks at some basic long-term mean tropospheric features (surface pressure, winds, temperature, and precipitation). Section 5 examines the simulation of the zonal-mean circulation in the middle atmosphere. Section 6 considers the model results for quadratic eddy terms as well as the zonal-mean radiative heating climatology. Section 7 documents the middle atmospheric stationary wave field in the NH winter. Section 8 is an investigation of the long period (semiannual through quasi-biennial) variations seen in the tropical middle atmosphere in the SKYHI integrations. Conclusions are summarized in section 9. Appendix A is devoted to an examination of the effects of recent model improvements on the SKYHI simulation. Appendix B discusses a parallel experiment conducted with the moderate-resolution SKYHI model but using a smoothed topography.

The results presented here in this rather broad survey of model performance will be somewhat descriptive. Many of the specific findings will raise questions that need to be addressed through more detailed analysis or particular model experiments. The present results should stimulate new developments in comprehensive atmospheric modeling and further research into the detailed dynamics of middle atmospheric circulation.

2. The SKYHI model formulation and the control integrations

a. *Basic features of the model*

The SKYHI model was developed from the 9-level latitude–longitude, sigma coordinate GCM described by Holloway and Manabe (1971, hereafter HM). The major developments from this model to the initial version of SKYHI are covered in Fels et al. (1980, hereafter FMSS). SKYHI retains the latitude–longitude nonstaggered grid and second-order horizontal differencing of HM. Zonal Fourier filtering of fields poleward of about 50° latitude is used to maintain a roughly isotropic horizontal resolution. The SKYHI model uses a hybrid vertical coordinate, which is terrain following near the ground, merging into pure isobaric coordinates above 321 mb. Centered second-order differences are used to approximate vertical derivatives for most terms. The only exception is in the vertical flux convergence of water vapor, which is done with a fourth-order scheme. This paper considers the same 40-level version discussed in previous papers (see FMSS for a complete listing of the levels). The lowest full model level is at roughly 80 m above the ground. The level spacing gradually increases with height and is very roughly 2 km through most of the stratosphere.

The traditional upper boundary condition is applied so that the vertical velocity is required to vanish at a half level formally located at zero pressure. In order to reduce reflection of vertically propagating waves from the model top, a linear damping of the deviation from the zonal mean is applied to the temperature and horizontal wind at the highest model full level (0.0096 mb). The timescale for this relaxation used in the present integrations is 10 800 s.

This paper will consider integrations performed with versions of the model with three different latitude–longitude resolutions: 1° × 1.2° ($N90$), 2° × 2.4° ($N45$), and 3° × 3.6° ($N30$), where N is the number of grid rows between the equator and pole. The model is integrated with a simple explicit leapfrog time differencing.

b. *Topography*

The topographic heights employed are based on the 1° × 1° dataset widely distributed by the Scripps Institute of Oceanography. These original data were interpolated in a straightforward way onto the 1° × 1.2° $N90$ grid. Then these $N90$ heights were averaged over the $N45$ and $N30$ grid boxes to produce consistent topographic heights at these lower resolutions. [Note that while the $N90$ topography has remained the same for all the SKYHI integrations conducted, the $N30$ topography used for the runs described in this paper is slightly different from that employed in most earlier publications such as Hamilton and Mahlman (1988), Hayashi et al. (1989), and Mahlman et al. (1994).] The result in each case effectively represents the observed topography simply averaged over each model grid box. This field is filtered in the zonal direction at high latitudes to be consistent with the Fourier filter used in the model but is otherwise unsmoothed. The use of unsmoothed topography distinguishes the SKYHI integrations described here from most other published GCM experiments. This approach has the disadvantage that it introduces variations in the boundary conditions even down to the two-grid length scale (for which derivatives are not well approximated by finite differences). However, the representation of one-

dimensional vertical processes presumably is more accurate when the realistic topographic height is used at each grid point. The amount of topographic smoothing adopted in a GCM is always somewhat arbitrary, and the present approach represents one extreme possibility. Figure 1 shows the SKYHI topography around latitude circles near 35°N in the three resolutions. At *N*90 resolution the topography is sufficiently rough that the model should explicitly represent some of the enhanced blocking of the flow that advocates of "envelope orography" have discussed (e.g., Wallace et al. 1983).

c. *Mixing parameterizations*

The basic subgrid-scale mixing parameterizations in the original SKYHI are described in FMSS and Levy et al. (1982). The vertical mixing consists of a second-order diffusion with a coefficient dependent on the model-resolved bulk Richardson number (Ri). The original FMSS version of SKYHI employed the standard Smagorinsky nonlinear horizontal eddy diffusivity described by HM. This was later modified by Andrews et al. (1983; see their appendix A).

d. *Surface physics*

The exchanges of heat, momentum, and water between the lowest atmospheric level and the surface are all parameterized with the standard bulk aerodynamic formulas (see HM). A minor modification is introduced to prevent the exchanges from becoming extremely small in weak wind conditions (the magnitude of the lowest-level wind, which appears as a factor in the standard formulas, is not allowed to drop below 0.1 m s^{-1}). There is also an enhancement of the surface exchanges when the potential temperature at the surface exceeds that in the lowest full model level.

The treatment of the surface heat balance over land and the calculation of the drag coefficient differ between the *N*90 and the lower-resolution models discussed in this paper. The *N*90 version retains the instantaneous heat balance (no net flux of heat into or out of the land surface) of the original HM and FMSS models. The drag coefficient C_D for the *N*90 version is specified simply as .003 over land or sea ice and .001 over open ocean. If the surface temperature is larger than the lowest model level temperature, then the values for C_D given above are multiplied by (U + 0.6)/U, where U is the magnitude of the lowest-level wind in meters per second.

The N30 and N45 integrations described in this paper are made with the first version of SKYHI to include an updated scheme for computing surface temperatures. This uses a prognostic equation for a single soil layer with heat capacity appropriate for a 0.10-m depth (and including a contribution from the soil moisture at each grid point). In addition, the new scheme uses Monin–Obhukov scaling to compute the transfers between the ground and the lowest model level (effectively, this amounts to a more sophisticated determination of the shear and stability dependence of C_D). The similarity functions and parameters are taken from Hicks (1976). A uniform roughness length of 0.1682 m is used for all land and sea ice points, while the roughness of the ocean depends on the overlying winds [following the formulation originally due to Charnock; see Eq. (33) of Delsol et al. (1971)].

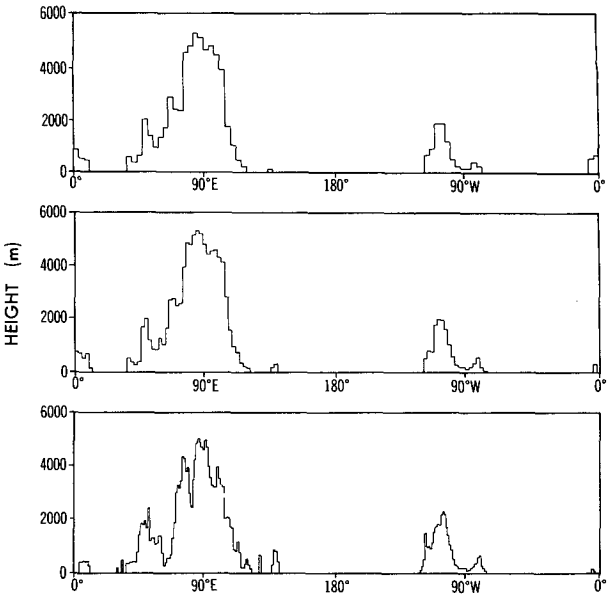

FIG. 1. Section of the topographic relief used in the three versions of the SKYHI model: *N*30 (top), *N*45 (middle), and *N*90 (bottom). The sections are through the grid rows centered at 34.5°N for *N*30 and *N*90 and through the grid row at 35°N for the *N*45 model.

In each case at ocean points the surface temperatures are specified as a function of time of year. The values used are taken from HM. The simple sea ice parameterization also follows HM and requires each ocean grid point to be either all open or all ice (which is assumed to be 2 m thick). The seasonal formation and disappearance of the ice is prescribed.

e. *Radiative transfer algorithms*

The SKYHI radiation code considers both the longwave and shortwave effects of O_3, H_2O, CO_2, and clouds and includes a parameterization of shortwave absorption by O_2. In the present integrations the diurnal averages of the shortwave heating rates are employed. The basic features of the radiation code are described in FMSS, and this "old" code was used for the first part of the *N*90 control run as described below. The last part of the *N*90 control run and the entire *N*45 and *N*30 integrations were conducted with a "revised" radiation code. The improvements over the old FMSS code are as follows, in decreasing order of expected significance.

(i) The diurnal averaging of shortwave heating in the new code is performed using a very accurate Gaussian integration over calculations at eight individual zenith angles between sunrise and sunset, rather than using the "diurnal average zenith angle" formulation of Cogley and Borucki (1976) originally employed by FMSS. This changes some stratospheric shortwave heating rates by as much as ~10%.

(ii) The original "*p*-type" H_2O continuum is replaced in the new code by an "*e*-type" continuum. This is effectively the change from Version I to Version II of the Fels–Schwarzkopf radiation model described in Fels et al. (1991).

(iii) The shortwave absorption by water vapor is now done using the improved method of Freidenreich and Ramaswamy (1993).

(iv) The CO_2 transmission functions in the longwave code have been replaced in the new version by the more accurate calculations of Schwarzkopf and Fels (1985).

(v) A modification of the source function for the CO_2 longwave computation is added to roughly account for non-LTE effects. This is applied only at the top three model levels (0.0697, 0.0308, and 0.0096 mb), and the actual effects at these levels are quite small.

f. Distribution of radiatively active species

The CO_2 volume mixing ratio is set to 330 ppmv uniformly. The water vapor is determined self-consistently throughout the model integrations. The only source for water vapor in the model is evaporation from the surface. The base ozone concentrations are specified as a function of pressure and latitude. The actual instantaneous ozone values above 7 mb are allowed to deviate somewhat from the base values depending on the local temperature (see appendix A of FMSS for details of this parameterization). The actual values for the temperature-dependent relaxation rates used in the FMSS version of this parameterization have since been updated on the basis of more recent photochemical model calculations.

The base ozone values are shown in Fig. 2.3 of FMSS and, below 10 mb, were derived from analysis of balloon-borne ozonesonde measurements. The values above 10 mb were based roughly on the limited satellite and rocket data then available. As explained in FMSS, the values were adjusted so that the simulated tropical temperature profile agreed well with observations. This produced an ozone distribution that has somewhat lower values in the middle and upper stratosphere than more recent satellite observations would suggest. The highest ozone mass mixing ratio in the SKYHI climatology is less than 15 ppmm. This compares with the maximum value of about 18 ppmm in the climatology of Keating and Young (1985), for example. Use of this adjusted SKYHI ozone climatology led to reasonable temperatures in the tropical stratosphere when the original Cogley and Borucki (1976) diurnal averaging scheme for the shortwave radiation was employed. However, with the change to the more accurate diurnal averaging in the present simulations, the low ozone concentrations result in a significant temperature bias in the simulated tropical upper stratosphere (see section 5 and appendix A). The cloud distribution and snow-free surface albedos are prescribed as in FMSS.

g. Moist convection and precipitation

At the end of each time step the model fields undergo moist and dry convective adjustment along with the production of stable rain. The basic scheme is as described in HM. The condensation criterion for the present model integrations is set at 85% of the saturation mixing ratio computed on the basis of the grid-scale temperature. No momentum is mixed in either the dry or moist adjustments (although the Ri-dependent vertical diffusion does mix momentum in dry convective situations). The first part of the *N*90 integration was conducted with a version of the moist convective adjustment routine that was later found to have a code error. The problem occurred in the table lookup for the saturation mixing ratio that was used in the calculation of the moist adiabatic lapse rate (but not in the computation of the actual condensation of water vapor and associated latent heat release). The values of saturation mixing ratio used were extremely low, so the moist convective adjustment effectively proceeded toward the dry adiabatic lapse rate. The effects of this error are discussed in appendix A. It appears that this same error was present in earlier versions of SKYHI run on the GFDL CYBER computer—that is, in papers published after Andrews et al. (1983) until the recent publications of Hamilton (1993a,b; 1994a,b), Manzini and Hamilton (1993), and Strahan and Mahlman (1994a,b), which all analyze results obtained with the error corrected. The error was corrected before the *N*30 and *N*45 control runs described in the present paper were begun.

h. The control integrations

One unusual feature of SKYHI is the use of an astronomically accurate dating system. Each day of each integration is assigned some date in the Gregorian calendar. The integrations of present interest have their ultimate origin in the experiment described in FMSS. This started in *1978* (hereinafter italic font will denote model years) from motionless isothermal conditions and employed a low–horizontal resolution version with annual-mean insolation. The water vapor mixing ratio was initially set to 2.5 ppmm everywhere. The annual cycle of insolation (and SST evolution) was activated on astronomical date 23 September *1981* when a 5° × 6° version (*N*18) was employed. The seasonally

varying *N*18 integration continued for a little over a year. On 30 September *1982* the fields from the *N*18 model were interpolated onto the *N*90 grid, and the present (seasonally varying) *N*90 SKYHI control integration began. This used the old FMSS radiation algorithms until 30 May *1983*, when the revised radiation began to be employed (the code error in the moist convection was corrected on the same date). The *N*90 control has now proceeded through September *1984*. The *N*90 fields on 6 June *1983* were interpolated onto *N*30 and *N*45 grids, and the present lower-resolution control runs were started. The *N*45 integration continued through January *1986*, and the *N*30 integration has continued past the year *2014*.

Roughly the first two years of the *N*30 integration were discarded, and analysis starts with data in *1985*. Thus, it is reasonable to expect the present *N*30 results to be essentially independent of the initial conditions. With the relatively short *N*45 and *N*90 runs, there is not the possibility of discarding such a long initial spinup period (the climatological results for *N*45 described in this paper are based on February *1984* through January *1986* data). This is a particular concern for the tropical stratosphere. It is reasonable to expect that throughout the present *N*90 integration, the circulation in the tropical stratosphere will be relaxing from the "shocks" introduced by the resolution change in September *1982* and the changes in model physics in May *1983*. For the most part, analysis of the *N*90 integration will use only results after 1 June *1983*.

3. Climatological data for model comparison

The extensive documentation attempted here for the SKYHI model will involve comparison with a number of observed fields. Unfortunately, there is no single climatology available that includes all the fields needed over the surface to 0.0096-mb domain of interest. In this section a brief description will be given of the most important datasets used for comparison with the model results.

The source for zonal-mean winds and temperatures was the compilation of Fleming et al. (1988, hereafter FCSB). This gives zonal-mean temperature and gradient balance winds from 1000 to above 0.01 mb for each month of the year. FCSB is based on Oort's (1983) analysis of radiosonde data up to 50 mb and on Barnett and Corney (1985a) above that level. Barnett and Corney (1985a) is based on Oort (1983) at 50 mb, subjectively analyzed radiosonde data from the Free University of Berlin at 30 mb, and about 5 years of IR radiometer data from two different satellites at higher levels. While a very valuable and convenient reference, the FCSB climatology does have some limitations. The values in FCSB are given at about 3-km vertical resolution, which is a particular problem when trying to determine the actual temperature near the tropopause. The zonal winds at low latitudes in FCSB are also very questionable, due to the use of gradient wind balance with rather low-spatial resolution temperature data. The equatorial middle atmospheric zonal winds in FCSB are generally weaker than those found in the detailed analysis of high-resolution satellite data by Hitchmann and Leovy (1986), in the climatology based on direct (rocket and radar) zonal wind measurements compiled by Kantor and Cole (1964), or in the analysis of data at individual low-latitude rocket stations discussed by Reed (1965), Hirota (1978), and Hamilton (1982b).

For most other tropospheric fields (including quadratic eddy quantities) the climatology of Schubert et al. (1990a,b—hereafter SMPSW) is used. This is based on eight years of ECMWF operational analyses and ranges over standard pressure levels from 1000 to 100 mb. Observed precipitation climatology is taken from the work of Legates and Willmott (1990). This provides rainfall rates for the whole globe within 0.5° latitude–longitude boxes. Over land each box value represents an average of multiyear means for all available stations (corrected for various biases in rain gauge measurements), while over the ocean more indirect methods are used to infer the precipitation rates.

The quadratic eddy quantities between 100 and 0.4 *mb* used in the present work are taken from Wu et al. (1987), which represents a four-year average of statistics based on daily NMC analyses. These NMC data were for only temperature and geopotential, so Wu et al. estimated the eddy winds using geostrophic balance. The climatology of Randel (1992), while not actually used in any of the present figures, will be another valuable reference for comparison. Randel (1992) derived zonal means and quadratic eddy quantities from eight years of NMC temperature and geopotential analyses. His results extend up to only 1.0 mb, however, due to his concern about the quality of the analyses above that level. Hamilton (1982a) presents yet another set of zonal-mean eddy statistics, in this case computed from four years of weekly subjective upper-atmosphere analyses up to 0.4 mb and based on both operational satellite radiometer data and meteorological rocket soundings.

Detailed horizontal sections of the geopotential for the NH at 100, 50, 30, and 10 mb will be used to characterize the lower-stratospheric stationary wave field. These were taken from the monthly means of the subjectively analyzed radiosonde data prepared at the Free University of Berlin and provided on the widely distributed GEDEX (Greenhouse Effect Detection Experiment) compact disc. There are 23, 34, 34, and 17 years of data provided for the levels 100, 50, 30, and 10 mb respectively.

4. Basic results for the troposphere

a. Surface pressure

Figure 2 shows the DJF mean sea level pressure (SLP) from observations (SMPSW) and from the *N*30,

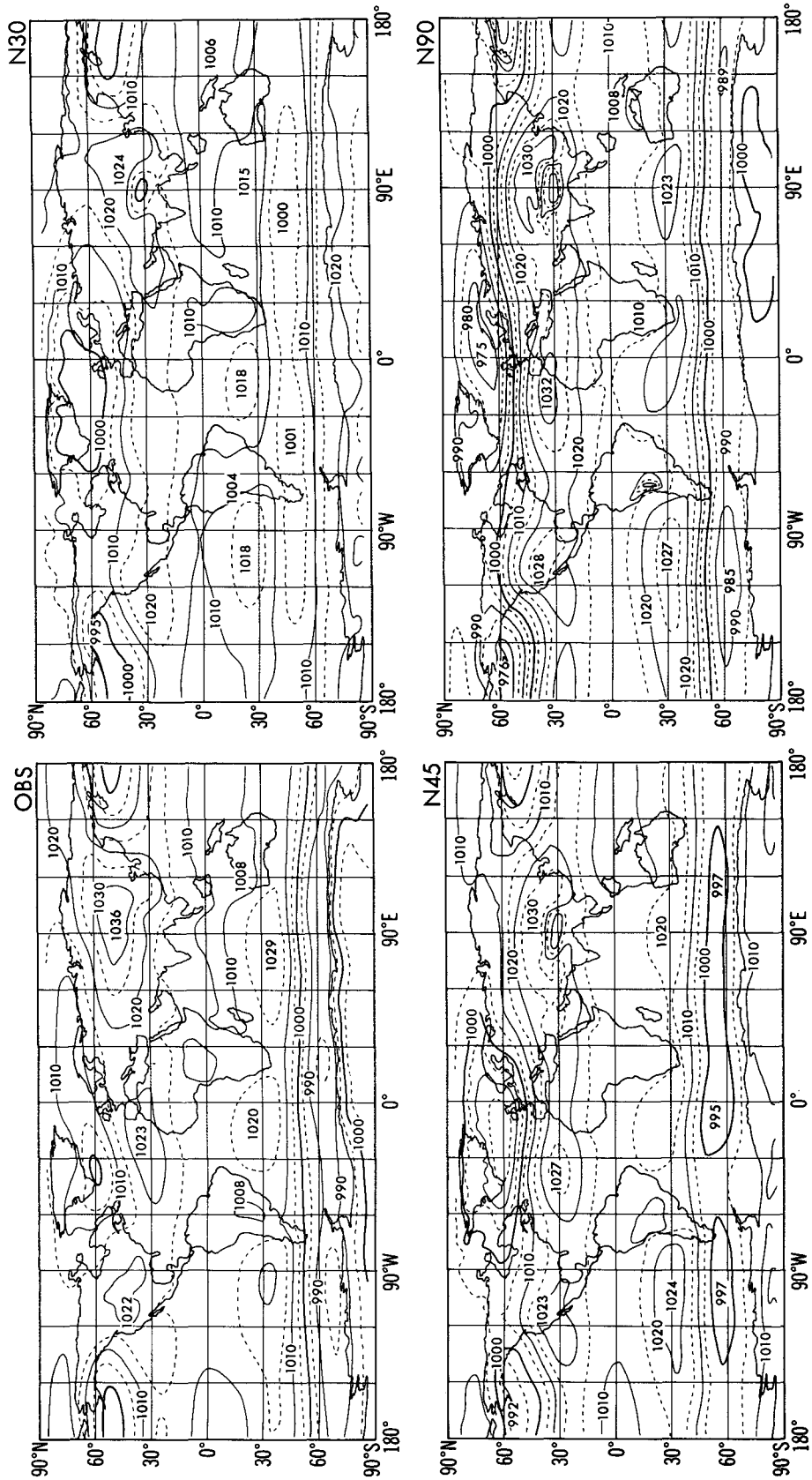

FIG. 2. DJF mean sea level pressure climatologies from observations and from the model control runs. The contour interval is 5 mb, and solid contours are used for values that are divisible by 10.

*N*45, and *N*90 simulations. The averaging period used is 10, 2, and 1 year for the *N*30, *N*45, and *N*90 integrations, respectively. Note that the extrapolation to sea level was presumably done differently in SMPSW and in the present model results (and so comparisons over the very high topography of the Himalayas and Antarctica may not be meaningful). The most notable feature is the strengthening of the zonal-mean gradients in the extratropics as the model resolution increases. This clearly occurs in both hemispheres, but to different effect. In the SH the intensification of the pressure gradients leads to good agreement between the *N*90 model and observations; but in the NH the meridional pressure gradients seen at *N*90 resolution are much too strong. Of course, one expects considerable interannual variability even in the seasonal mean SLP, and this complicates the comparison with a single winter of *N*90 data. The *N*90 simulated SLP distribution for the previous winter (i.e., DJF *1982/83*) was also examined (not shown), and the meridional gradient was again found to be much stronger than in the long-term mean observed climatology. The results for *1982/83* and those in Fig. 2 can also be usefully compared with the sequence of 34 individual yearly observed DJF pressure maps for the eastern Pacific/North American sector published in Emery and Hamilton (1985). In none of the observed winter means is the Aleutian low as intense (<980 mb) as in either of the two *N*90 winters.

A similar comparison has been made of the SLP from observations and from the three different model simulations for the JJA period. The results in the NH in this case are somewhat less sensitive to resolution than in SH summer. The high pressure centers over the North Pacific and North Atlantic tend to strengthen somewhat with resolution, however, and are perhaps most realistically simulated at *N*90 resolution. By contrast, the effect of resolution in the winter hemisphere is very dramatic. Figure 3 shows the JJA SLP in a SH polar projection. At *N*30 the pressure gradients around Antarctica are unrealistically weak. This gradient intensifies with resolution until in the *N*90 simulation the results are fairly realistic. This emphasizes the severe problems in the *N*30 simulation. Remarkably, in the *N*30 climatology there are almost no surface westerlies over the circumpolar ocean in the sector bounded by 120°E and 120°W. While the situation is improved in the *N*45 SKYHI, only at *N*90 resolution do the pressure gradients in this hemisphere come close to those observed. As will be shown below, this dramatic improvement at *N*90 is paralleled in other aspects of the simulated SH meteorology.

The behavior of the surface pressure field in the SKYHI model as a function of horizontal resolution has parallels in other GCM simulations, which do not include subgrid-scale gravity wave drag (e.g., Manabe et al. 1979; McFarlane 1987). Useful comparisons may also be made with some published studies of models that do include gravity wave drag. In particular, Boer and Lazare (1988) considered DJF simulations in a spectral model with triangular truncation at T20, T30, and T40 resolution, and Boville (1991) considered DJF simulations at T21, T31, T42, and T63 resolution in a model with essentially the same gravity wave drag parameterization as employed in Boer and Lazare. It is interesting that Boer and Lazare find that, over most of the globe, they are able to keep the basic features of the DJF SLP simulation similar at all three resolutions. However, their results in the SH circumpolar ocean region closely parallel the present findings; that is, there is a systematic intensification of the meridional SLP gradient with increasing resolution (see their Fig. 1). Boville (1991) finds similar effects in the SH circumpolar ocean region. However, Boville finds that even with gravity wave drag his DJF mean SLP climatology also significantly changes with resolution in the NH, and that the most realistic results occur at his highest resolution.

The overall tendency for the strengthening of horizontal SLP gradients with increasing horizontal resolution is apparently present in all GCMs. However, the details of the resolution dependence vary greatly among different models. One encouraging aspect of the SKYHI results is that at high resolution the circumpolar SH simulation is quite realistic, while the overly intense NH surface westerlies could presumably be corrected by the addition of some topographic gravity wave drag.

b. Upper-level flow

Figure 4 shows the DJF climatology for the 200-mb zonal wind from observations and from the three SKYHI resolutions. Most aspects of the observed geographical pattern are reasonably well captured in all the model simulations. In particular, the intensification of the wind in the eastern North America/North Atlantic and East Asian/North Pacific jets is evident in all the models. The simulation appears to change somewhat with resolution, but the effects are much less dramatic for the upper-level winds than for the SLP. The general effect of increasing resolution is to intensify meridional contrasts and thus make the jet features more zonally elongated. The simulation of the East Asian jet appears to be clearly improved by the increasing resolution. The elongation of the North Atlantic jet may be somewhat too great in the *N*90 model. The extent of the region of tropical easterlies appears to be somewhat closer to observations in the *N*45 and *N*90 models than in *N*30.

Figure 5 shows the 200-mb zonal wind comparisons for JJA. The SKYHI results in the NH seem to improve with resolution. In particular the observed jet over North America and the North Atlantic indicated in observations becomes much more clearly defined in the simulation as the model resolution increases from *N*30 to *N*90. The magnitude of the wind in the East Asian jet is also improved in the *N*90 model over that seen at lower resolutions. In the SH the simulation is appar-

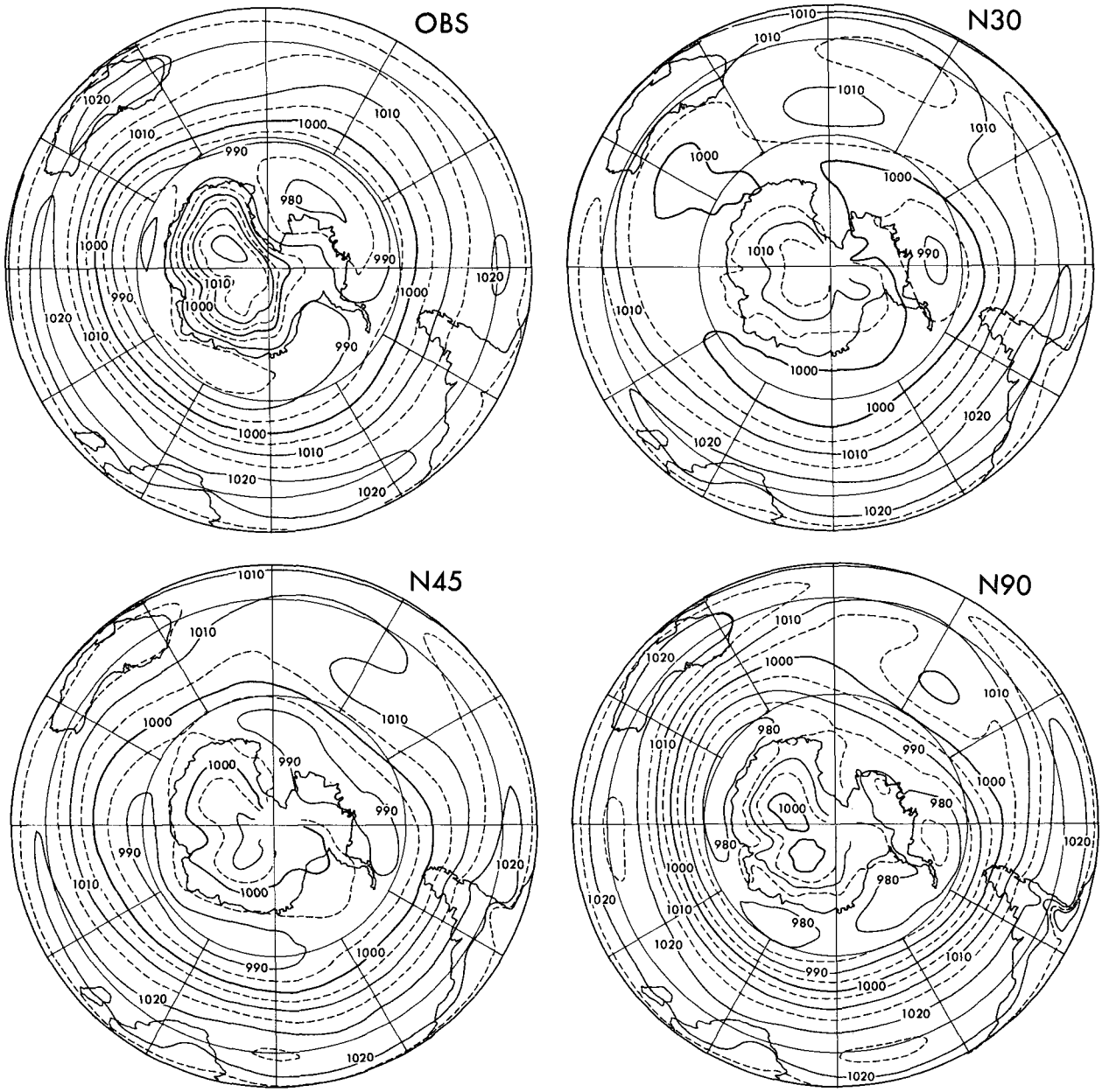

FIG. 3. As in Fig. 2 but results for JJA presented for the SH.

ently not as sensitive to resolution, except in the circumpolar ocean areas. Here the *N*30 model may somewhat underestimate the zonal winds (consistent with the weak circumpolar circulation simulated near the surface), while *N*90 comes closer to simulating the observed very strong winds.

c. *Precipitation*

The annual-mean precipitation rate over land is shown in Fig. 6 for observations (Legates and Willmott 1990), and for each of the three SKYHI control runs. The model results represent 10-, 2-, and 1-year means for the *N*30, *N*45, and *N*90 resolutions, respectively, but no spatial smoothing has been applied to any of these fields. It is evident that the raw SKYHI model precipitation fields are quite smooth, and the simulation does not appear to suffer from the small-scale geographically fixed variations in precipitation that many spectral models display. The overall simulation is reasonably good in all three versions of the model, but there are some obvious deficiencies in specific areas. In partic-

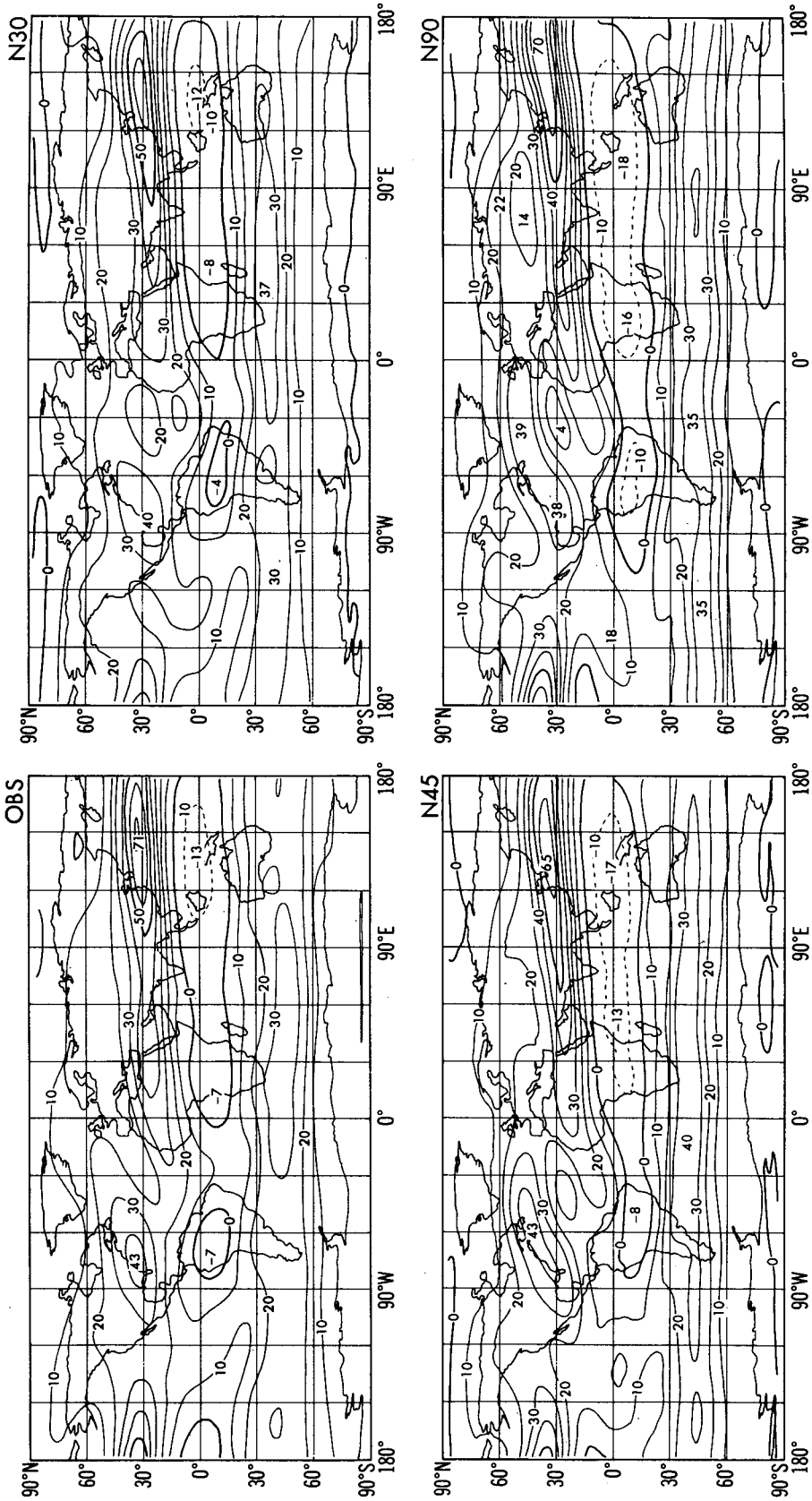

FIG. 4. DJF mean 200-mb zonal wind climatologies from observations and from the model control runs. Contour interval is 10 m s^{-1}, and dashed contours denote easterly winds.

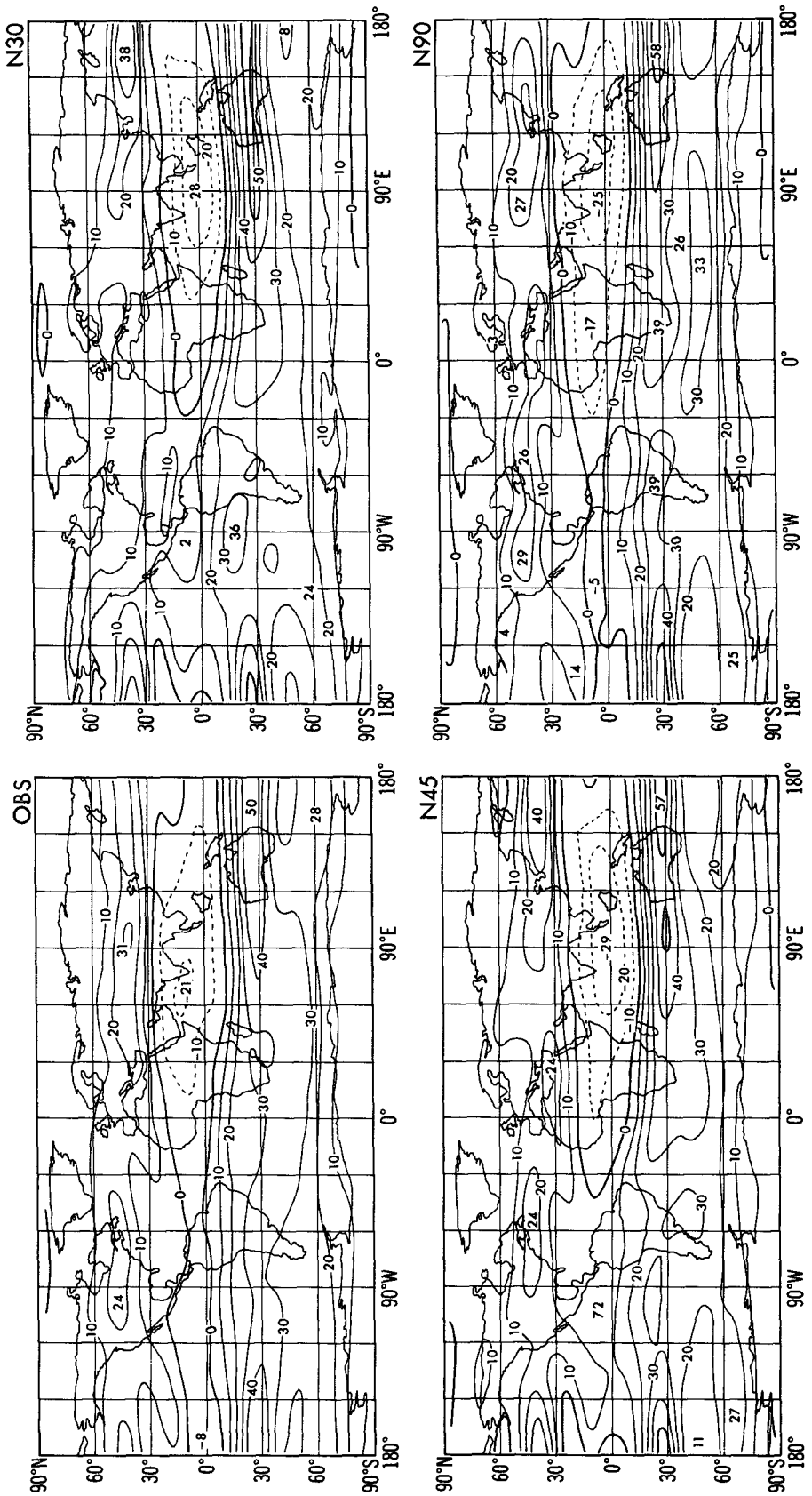

FIG. 5. As in Fig. 4 but for the JJA mean.

FIG. 6. Annual-mean precipitation rate climatologies from observations and from the model control runs. The key to the shading is labeled in mm d^{-1}. Results shown only for land areas equatorward of 60° latitude. The model fields are unsmoothed and plotted at the model resolution in each case. The observations are from Legates and Willmott (1990), but their 0.5° × 0.5° data have been averaged into 1° × 1.2° grid boxes before plotting.

ular, all three resolutions underestimate the extent of the central Asian desert region. Much of the interior of Asia as well as the southern end of the Arabian peninsula is unrealistically wet in the model simulation. The intense rainfall in Southeast Asia is clearly present in the model results, but the rainfall in northern India is greatly underestimated. This particular problem (i.e., having a reasonable Southeast Asian monsoon but a very poor Indian monsoon) afflicts many other GCMs as well (e.g., Zwiers 1993). Another obvious problem in SKYHI is the overly wet simulation in the western United States. It is striking that the model results are relatively insensitive to resolution, and particularly that none of the most obvious model deficiencies are remedied by increasing resolution.

Figure 7 shows the same precipitation comparison over the oceans. The near-equatorial rainband and the subtropical dry areas are well represented in each of the three models. The enhanced rainfall along the North Pacific and North Atlantic storm tracks is present in the model, but the simulated precipitation rates are smaller than observed. The precipitation along the storm tracks is one aspect of the simulation that does seem to be improved in the *N*90 resolution SKYHI. The model simulation (which has no interannual SST variations) over the tropical Pacific must be regarded with particular caution, since the actual precipitation in this region varies enormously through each cycle of the Southern Oscillation.

Hulme (1991) has recently computed an objective measure of the quality of a model precipitation climatology as the (area weighted) correlation coefficient between the observed and model annual-mean precipitation rates as averaged in 5° × 5° latitude–longitude boxes. He chose only to consider boxes consisting primarily of land points (and he ignored a small number of boxes where the data were not available in some of the observed climatologies he considered). He applied this method to several state-of-the-art climate GCMs and found a range of correlations between 0.60 and 0.84 (when the Legates and Willmott climatology was used for the observations).

As part of the present study essentially the same quantity was computed for the correlation between the SKYHI simulations and the Legates and Willmott climatology. The first step in this procedure was to put the observed as well as each of the model-simulated annual-mean precipitation rates onto the 1° × 1.2° *N*90 grid. The correlation coefficients calculated over all the land points of this grid are given as the "unsmoothed" values in the first line of Table 1. The computation was then repeated, but with the precipitation rates first binned into 5° × 6° boxes. These are the "smoothed" values in Table 1 and should be directly comparable to the results of Hulme (1991). The results for the smoothed fields (0.78, 0.76, and 0.82 for *N*30, *N*45, and *N*90, respectively) are in the upper range of those obtained by Hulme for several other GCMs. It is interesting that the correlations computed over the fine 1° × 1.2° grid are not much lower than those for the "smoothed" values. This demonstrates the rather smooth nature of the precipitation field produced by the SKYHI model. The second line of Table 1 gives the same correlation coefficients, but for the whole globe (land and ocean). The global correlations are somewhat reduced from those computed using only land points. This could reflect inadequacies in the oceanic observed climatology, of course. The final two lines show results of repeating the land and the land plus ocean calculations when attention is restricted to the region equatorward of 30° latitude. The lowest values for all three models are for the land plus ocean low-latitude region. It remains to be seen how much the imposition of a realistic interannual SST variation in the model might improve the low-latitude results.

As expected from Figs. 6 and 7, the annual-mean precipitation simulations at different resolutions are well correlated. The global correlation coefficient between the *N*30 and *N*45 simulation is 0.94, while that between the *N*30 and *N*90 results is 0.87.

Figure 8 shows the *N*30 continental precipitation comparison with observations for the DJF and JJA periods. The model successfully reproduces the basic seasonal march in the Tropics, notably the northward shift of the heavy precipitation belts over Africa and South America from DJF to JJA. The problems in simulating the Indian monsoon are very clearly exposed in the JJA results, however. In both the tropical and extratropical NH the DJF simulation appears to be more realistic than the that for JJA. In particular the observed pattern of precipitation over North America is well captured by the model in DJF, but not in JJA. This impression is confirmed by computations of the correlation coefficients. The seasonal-mean correlation coefficients with the Legates and Willmott observations are shown in Table 2 for each of the models (using the 5° × 6° boxes for the correlation in each case). The correlation coefficients considering only NH land are larger in DJF than in JJA, at all SKYHI resolutions.

Overall, the SKYHI precipitation simulation is comparable to that of the best currently available GCMs. There is obviously room for significant improvement, however. The fact that the main deficiencies in the simulated precipitation field are in the Tropics and in the summer extratropics (i.e., where the solar zenith angles are low and the direct surface heating is large) may reflect deficiencies in the very simple surface physics and/or the prescribed cloudiness in the model. The summer and tropical precipitation simulations are presumably quite sensitive to the representation of the land–sea contrasts in heating. The oceanic heating should be taken care of by the prescribed surface temperatures, but the amount of heating over land depends on the formulation of radiative effects and the surface heat balance. The fact that the model as a whole has a tropospheric cold bias (see section 4d) provides evi-

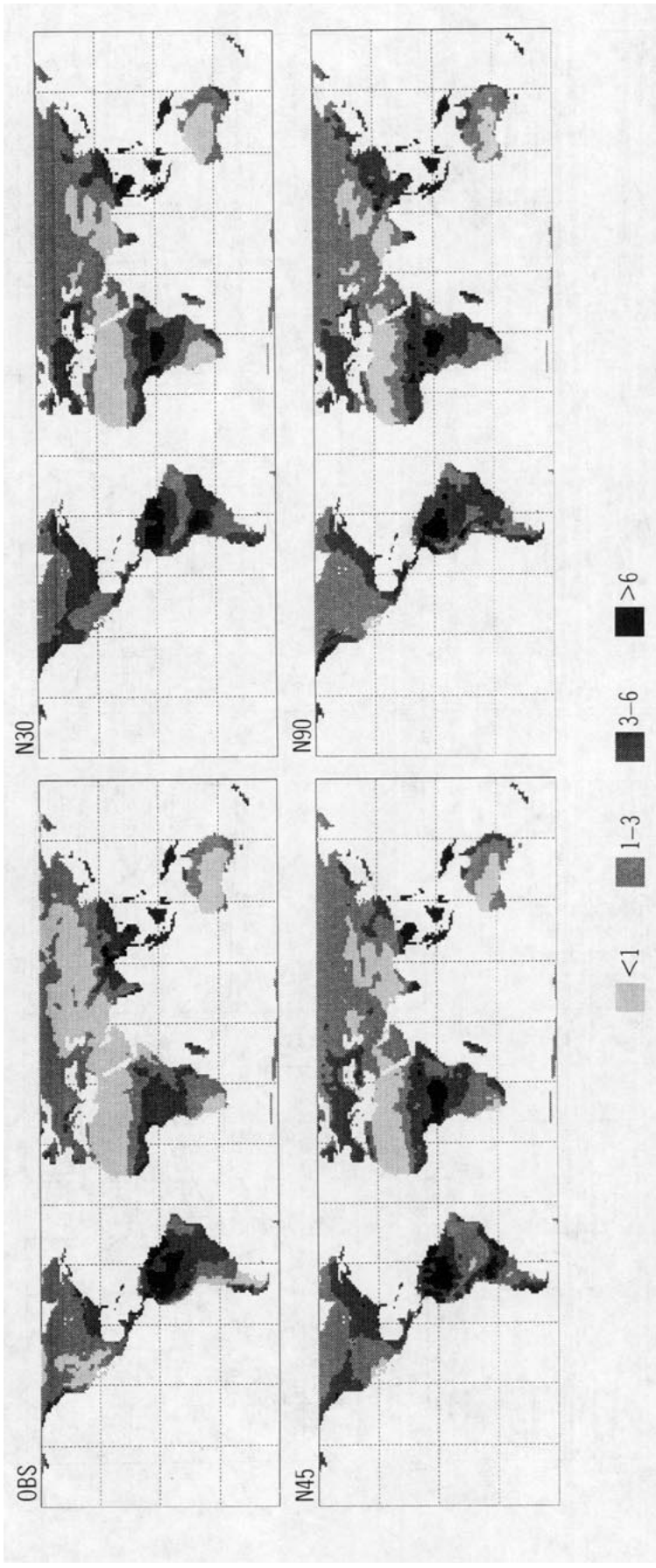
OBS
N30
N45
N90
<1
1–3
3–6
>6

TABLE 1. Correlation coefficients between annual-mean rainfall in observations and in the SKYHI simulations. Unsmoothed values are for 1° × 1.2° grid boxes, while smoothed values are for 5° × 6° grid boxes. Low latitude refers to all grid boxes between 30°S and 30°N

	Unsmoothed			Smoothed		
	*N*30	*N*45	*N*90	*N*30	*N*45	*N*90
Global land	0.74	0.70	0.73	0.78	0.76	0.82
Global land and sea	0.68	0.63	0.67	0.71	0.69	0.73
Low-latitude land	0.72	0.66	0.68	0.77	0.72	0.79
Low-latitude land and sea	0.65	0.57	0.62	0.68	0.64	0.68

dence that the treatment of tropospheric heating is not adequate. The present results also should be considered in light of the recent study of Miller et al. (1992), who found that the tropical precipitation simulated in the ECMWF model was strikingly sensitive to fairly modest changes in the parameterization of evaporation.

d. Zonal-mean wind and temperature

Figure 9 shows the DJF climatology of zonally averaged zonal wind from the model and from observations (FCSB). The position and intensity of the NH subtropical jet stream is well simulated in all three models. The NH surface westerlies are already too strong in the *N*30 simulation and obviously increase still further with improved model resolution (in accord with the results in Fig. 2 above). The tropical upper-tropospheric westerly bias, which is clearly present in the *N*30 SKYHI, appears to be largely eliminated in the higher-resolution models. In the SH the westerly bias in the model is evident even at the core of the subtropical jet. The bias increases with increasing resolution. The position of the SH subtropical jet is also affected by resolution; the *N*30 results show the jet too far equatorward, but this bias is reduced at *N*90 resolution.

Figure 10 is a representation of the zonally averaged DJF temperature in the observations of FCSB and in the three SKYHI control runs. The observed temperatures are plotted in the upper left corner, and the other three panels show the deviation of the model climatology from the observations. In the troposphere the most notable feature in this figure is the considerable (over 5°C in some places) cold bias in all the model simulations. A part of this bias can be reasonably ascribed to the omission of trace constituents such as N_2O and chlorofluorocarbons from the radiative calculations (Wang et al. 1991). The bias is also no doubt related to the prescribed cloud distribution adopted. The present results may also indicate the need for a more penetrative convection scheme that could transport heat into the atmosphere more efficiently.

Figures 11 and 12 show the observed and simulated zonal winds and temperatures for the JJA period. As in the case of the DJF season, the SH tropospheric zonal westerlies are slightly stronger than indicated in FCSB. The tropospheric cold bias also is clearly present in JJA.

e. The tropical tropopause

The fact that the tropospheric cold bias noted in the previous section extends up to the tropopause is a particular concern for modeling of the stratospheric water vapor field, since the humidity of the air entering the stratosphere may be largely controlled by the saturation values at the tropopause cold trap. The thin curves in Fig. 13 show the long-term mean DJF 103-mb temperature along the equator in the *N*30, *N*45, and *N*90 models. For the construction of this figure the *N*30, *N*45, and *N*90 climatologies are based on 25, 2, and 1 year of data, respectively. There is only very slight interannual variability in the model simulation of this quantity, and both the *N*90 and *N*45 results stand out clearly when plotted with the 25 individual *N*30 winters. In order to make the *N*30 and *N*90 results as directly comparable as possible, the "equatorial" temperature is defined as the average over the two nearest grid rows (centered at 1.5°N and 1.5°S) for *N*30 and over the six nearest grid rows for *N*90.

The heavy curve in Fig. 13 is an attempt to show the 100-mb equatorial temperature from observations. It was based on the 100-mb contour plot in Newell et al. (1972), which itself was constructed by subjective analysis of radiosonde data. There is a comparable contour plot of DJF 100-mb temperature given by Oort (1983), based on his objective analysis of 15 years of radiosonde data. While over most of the Tropics Oort's result is very similar to that of Newell et al., Oort's analysis does indicate temperatures ~2°C warmer over the eastern Pacific (i.e., around 180° to 80°W, where there is very little data in any event).

Examination of Fig. 13 confirms the large discrepancies between the model temperatures and those observed. The longitudinal dependence of the temperature in the model has some similarity to that observed, at least to the extent that the lowest temperatures are located over the western Pacific. It is quite possible that the smoother variation seen in the observed curve simply reflects the lack of low-latitude observing stations. The model result—with three temperature minima corresponding to maxima in the convection over Africa, the eastern Pacific, and South America—is quite plausible. The minimum temperatures near 160°E are about 6° and 4° colder than observations in the *N*30 and *N*90 simulations, respectively. It is interesting that the improvement in the *N*90 simulation is not confined to the equator but appears over the entire Tropics (not shown). The difference among the three different SKYHI resolutions cannot be due to the direct radiative effects of clouds, since the cloud fields are identical in each case. One can speculate that, given the familiar tendency for convective instability to intensify at small

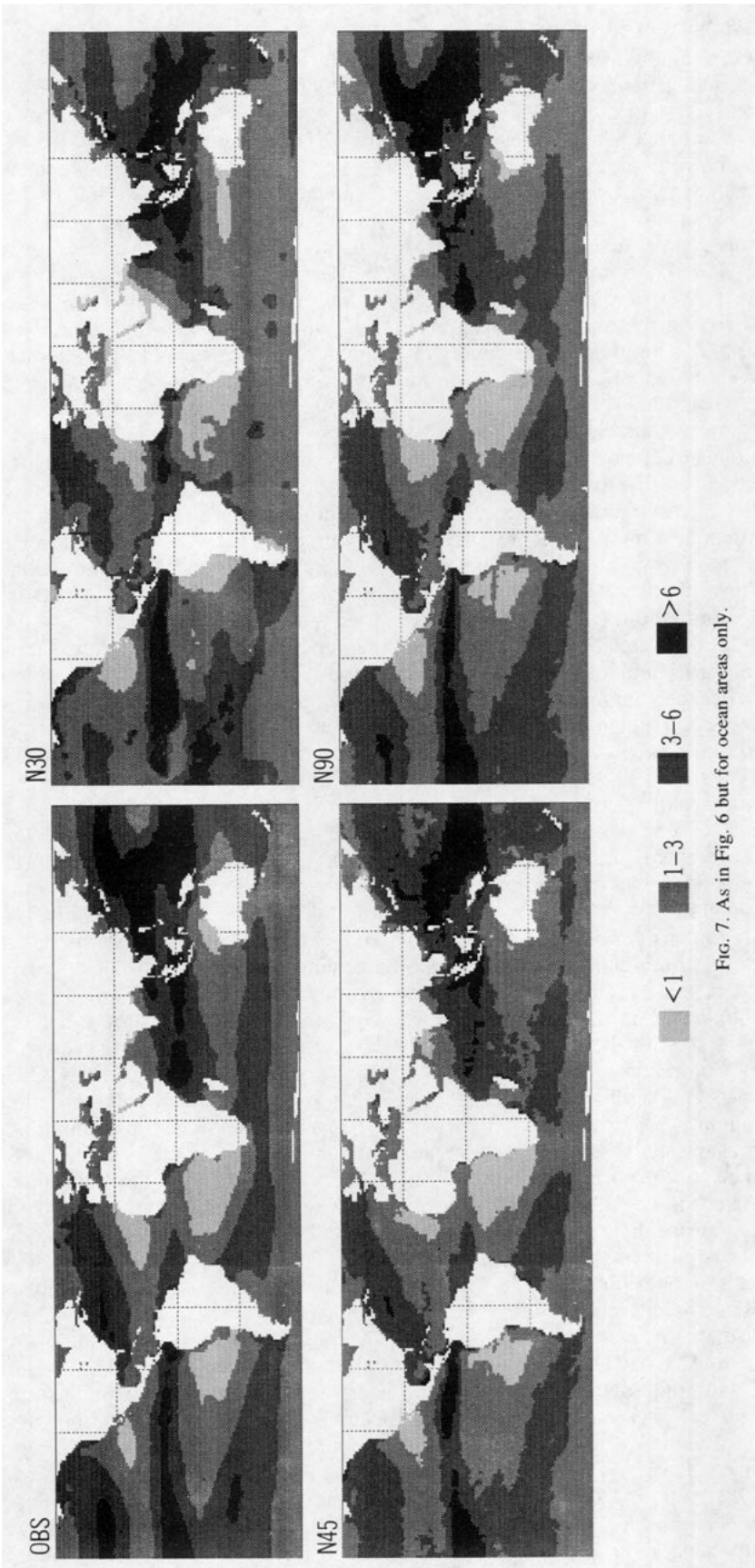

FIG. 7. As in Fig. 6 but for ocean areas only.

FIG. 8. DFJ and JJA mean precipitation rate climatologies from observations and from the *N*30 control run. The key to the shading is labeled in mm d^{-1}.

TABLE 2. Correlation coefficients of seasonal-mean precipitation in observations and in the SKYHI control runs. Smoothed values are used.

	DJF			JJA		
	*N*30	*N*45	*N*90	*N*30	*N*45	*N*90
Global land	0.83	0.82	0.86	0.62	0.61	0.71
NH land	0.88	0.85	0.81	0.56	0.53	0.65
SH land	0.77	0.75	0.82	0.70	0.80	0.86
Global land and sea	0.68	0.65	0.70	0.58	0.58	0.62
NH land and sea	0.76	0.74	0.73	0.56	0.55	0.59
SH land and sea	0.63	0.58	0.69	0.50	0.55	0.64

horizontal scales, there may be more deep convection (and hence more heating of the upper troposphere) when the model resolution is increased. Indeed, the zonal mean of the heating from subgrid-scale convection parameterizations in the tropical upper troposphere is larger in the *N*90 model than in the *N*30 model. It is possible that this effect might be less apparent if another convection parameterization were to be used, but the present results clearly emphasize the difficulty in formulating resolution-independent model parameterizations.

5. Zonally averaged circulation in the middle atmosphere

a. Northern Hemisphere winter simulation

The SKYHI DJF zonal wind and temperature cross sections in Figs. 9 and 10 display a number of interesting features in the stratosphere and mesosphere. The polar night jet in each of the model simulations is in reasonable agreement with observations in the lower stratosphere (below ~10 mb), but discrepancies become significant above this level. In particular, the model results have a vortex that is too strongly confined to high latitudes compared with the observations. This problem in the wind field is accompanied by a cold bias at high latitudes and a warm bias in the midlatitude band of the winter hemisphere (Fig. 10). The simula-

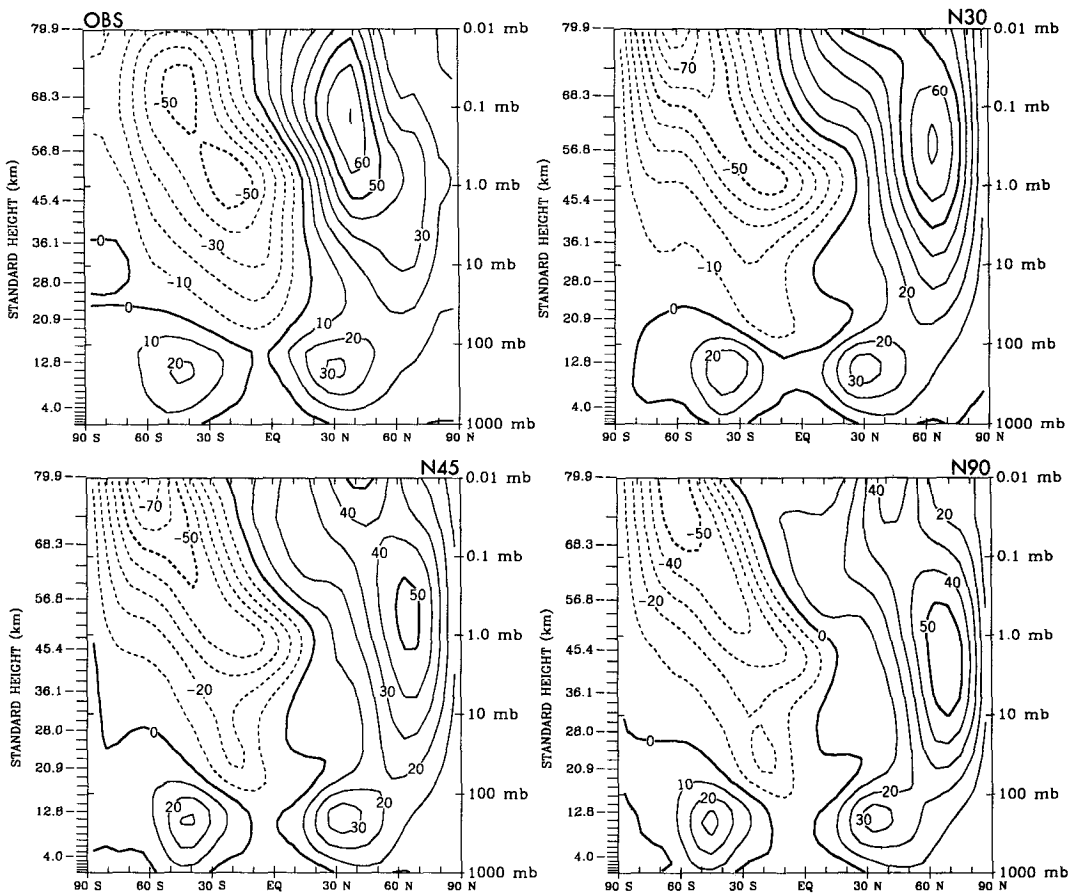

FIG. 9. DJF mean zonally averaged zonal wind climatologies from observations and from the model control runs. The contour interval is 10 m s^{-1}, and dashed contours denote easterly winds. The tick marks on the left show the locations of the 40 SKYHI model levels.

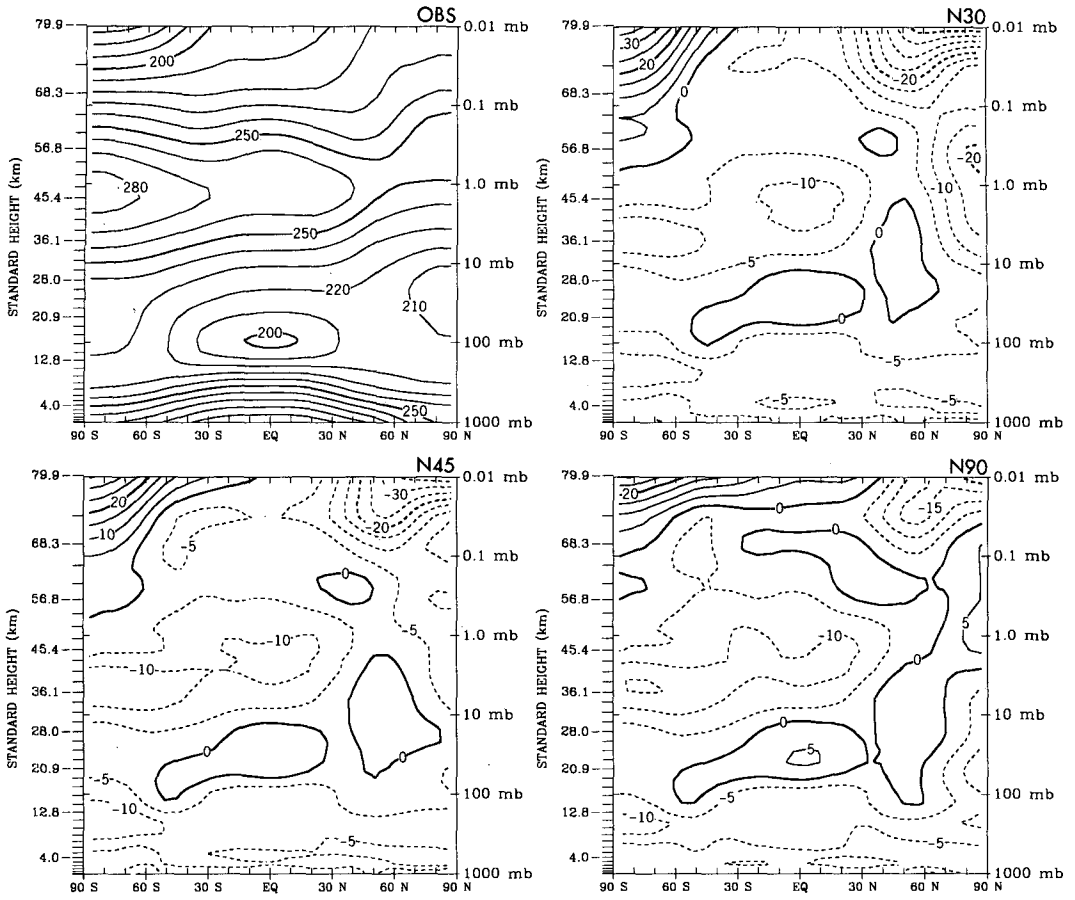

FIG. 10. The top left panel shows the DJF mean zonally averaged temperature from observations (CI: 10 K). The other three panels show the difference of the model climatologies from these observations. The contour interval in these panels is 5°C, and dashed contours denote regions where the model temperatures are lower than observed.

tion in this respect appears to be somewhat improved in the *N*45 and *N*90 results, but it is not clear that this difference is significant, given the large interannual variance seen in boreal winter in the *N*30 integration (see Hamilton 1994).

As noted earlier in section 3, the observed winds shown in Fig. 9 (and Fig. 11) are suspect in the tropical middle atmosphere. The actual zonal winds near the equatorial stratopause are almost certainly larger than those indicated in the FCSB data. The basic results in Fig. 9 for the model are in reasonable agreement with the January observations from Kantor and Cole (1964; see their Fig. 2). In particular, the Kantor and Cole observed cross section, like the model DJF simulation, displays an intense easterly tongue confined in altitude and centered around 1 mb (~50 km), which intrudes from the summer into the winter hemisphere. Further consideration of the tropical mean wind simulation in the model is postponed until section 8.

The low-latitude temperatures in the three models all have a consistent cold bias in the upper stratosphere, peaking at more than 10°C near 2 mb. There is also a warm bias in the lower stratosphere reaching as much as 5°C near 50 mb. These biases were much smaller in the model before the changes were made in the radiation routines (see appendix A). Compared with the old scheme, the new (and more accurate) diurnal averaging procedure for the shortwave radiation allows deeper penetration of the solar beam and hence less solar heating of the upper tropical stratosphere. As described in section 2, the prescribed ozone distribution in the model was designed to produce good simulations of the tropical middle atmospheric temperature (using the old radiation code). If this procedure were to be repeated with the improved radiation code, then higher ozone concentrations would clearly be required in the upper stratosphere and mesosphere (this would bring the ozone distribution more into line with current satellite-derived observational climatologies).

b. Southern Hemisphere winter simulation

The SH JJA simulation documented in Figs. 11 and 12 obviously has some serious deficiencies. At all three

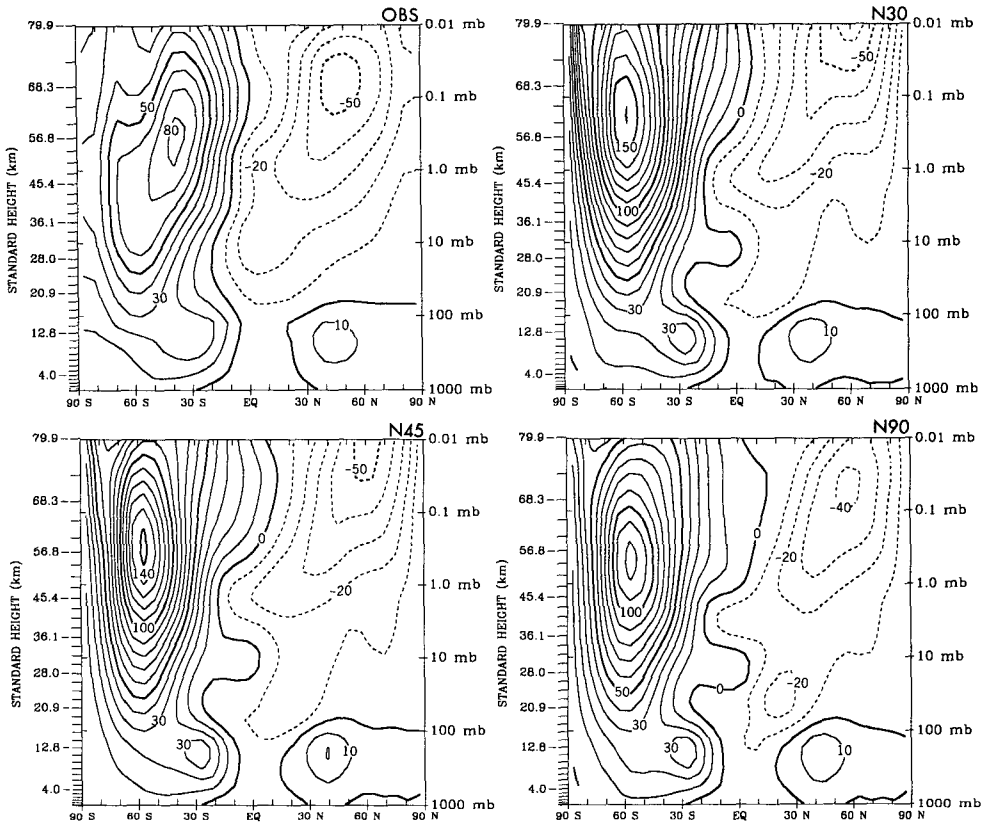

FIG. 11. As in Fig. 9 but for the JJA climatology.

resolutions the polar vortex is much too intense and centered at too high a latitude, particularly in the upper stratosphere and mesosphere. The polar temperatures in the model are much too cold, particularly in the upper stratosphere and near the stratopause. Both these problems are considerably reduced at higher resolution, although even at *N*90 resolution the discrepancies are still large (more than 30°C at 3 mb near the South Pole). The differences among the three versions of the model depicted in Fig. 12 (and the difference between the simulations and observations) are almost certainly significant [the interannual standard deviation in the observed high-latitude SH JJA temperature at 3 mb is less than 3°C; see Randel (1992)]. The implications of this apparent improvement of the simulation with resolution will be considered in section 6.

While the most striking aspect of Figs. 11 and 12 is the cold pole problem in the upper stratosphere and mesosphere, it is worthwhile to emphasize the fairly reasonable simulation in the SH lower winter stratosphere. Below about 20 mb the simulated temperatures are within 5°–10°C of observations [consistent with the results reported by Mahlman et al. (1994), who compared a 6-year mean of an earlier *N*30 integration with the observed climatology of Randel (1992)]. However, these biases are indications of important deficiencies in the vortex dynamics (see Strahan and Mahlman 1994a,b). The cold pole problem is manifested in the SH spring as a considerable bias (>1 month) in the timing of the breakdown of the winter polar vortex (Mahlman et al. 1994).

The tropical temperature biases in the JJA simulation are very similar to those in the DJF period (compare Figs. 10 and 12).

c. *NH and SH in summer*

Observations suggest that the summer polar mesopause may be the coldest region of the atmosphere (e.g., Lubken and von Zahn 1991). Given the reasonably strong radiative heating anticipated at the summer pole, the explanation for the observed mesopause temperature must involve a strong, dynamically driven residual circulation. Since only gravity waves are expected to have significant eddy transports in the summer middle atmosphere, the observed mesopause temperature presumably results from a balance between radiative heating and the residual circulation induced by the Eliassen–Palm (EP) flux divergence associated with the gravity wave field. Thus, assuming a GCM has an adequate representation of radiative processes in the upper mesosphere, the simulation of the summer

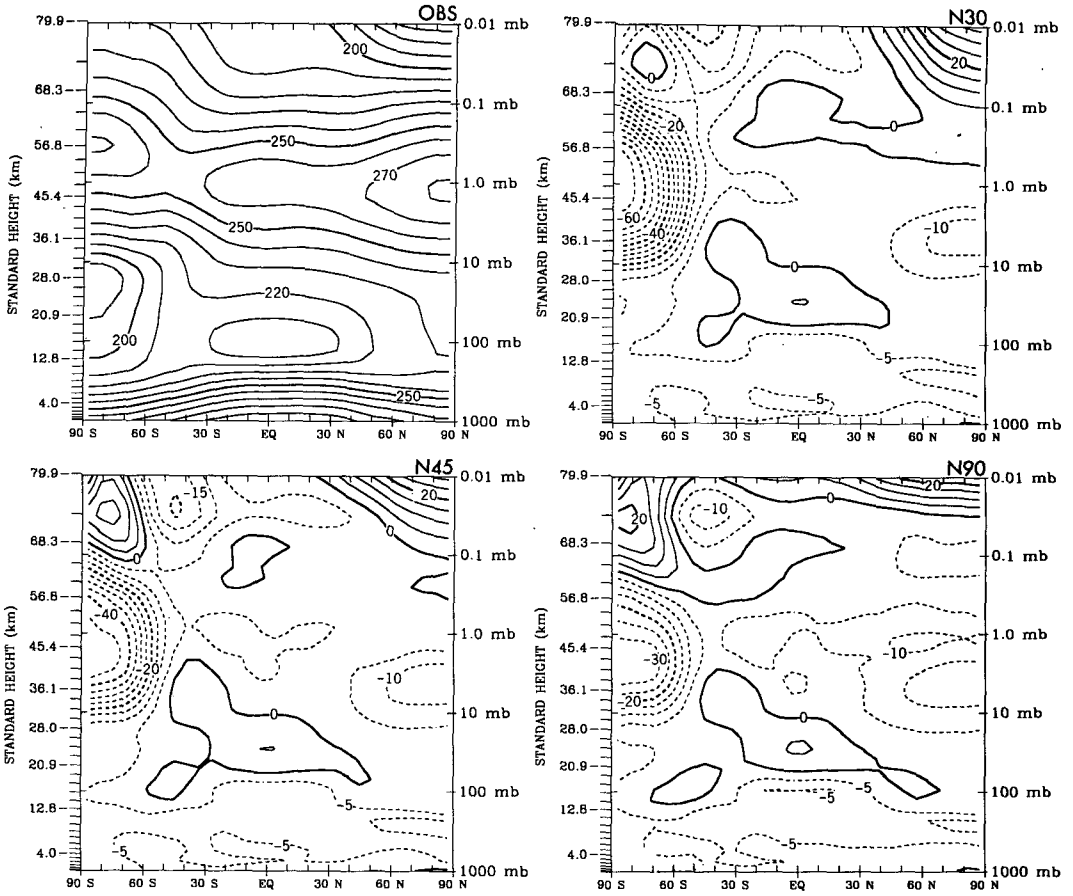

FIG. 12. As in Fig. 10 but for the JJA climatology.

polar mesopause temperature is a test of the model gravity wave EP fluxes.

The model simulation in the summer SH (Figs. 9 and 10) and in the summer NH (Figs. 11 and 12) will be considered together. For both cases, the overall position and strength of the summertime easterly jet are quite well simulated by each of the model resolutions, except in the upper mesosphere. Observations indicate that the jet actually closes off below the mesopause. This is accompanied by a very cold summer polar upper mesosphere [<170 K at the 0.01-mb level according to FCSB; recent observations suggest the possibility of even colder temperatures—Lubken and von Zahn (1991)]. The SKYHI model manages to produce a rather cold polar temperature, but not as cold as observed. The summertime easterly jet in the model also does not close off by 0.01 mb (except in the *N*90 JJA case). This discrepancy systematically improves with model resolution, however. The temperature at the 0.01-mb level at the summer pole is warmer than indicated in FCSB by about 35°C in the *N*30 simulation, 30°C in the *N*45 simulation, and 25°C in the *N*90 simulation.

Hayashi et al. (1989) noted that the circulation of the SKYHI model middle atmosphere included significant contributions from gravity waves of all resolved scales. As the model grid spacing is decreased a larger wavenumber range can be resolved and dissipation in the intermediate wavenumber bands is reduced, leading to increased vertical EP fluxes. The behavior seen in the mesosphere in the present simulations appears consistent with this earlier finding. The improvement in simulation of zonal-mean temperature with resolution is accompanied by clear increases in both the EP flux divergence and the transient eddy kinetic energy in the high-latitude upper mesosphere (see section 6). Given the deficiencies in the simulation even at *N*90 resolution, it seems clear that this process has not converged. However, the apparent tendency of the simulation to converge toward a realistic state suggests that a GCM with somewhat finer resolution could adequately simulate the mesospheric circulation without any additional parameterized drag. Of course, the problems in the temperature simulation near the summer mesopause reflect not only the inadequacies of the gravity wave simulation but also possible distortion of the mean me-

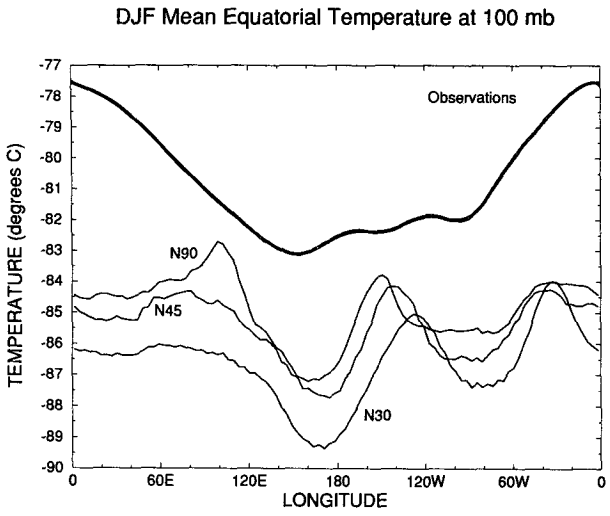

FIG. 13. The DJF mean equatorial temperature climatology at 100 mb from observations (data from Newell et al. 1972) and from the *N*30, *N*45, and *N*90 SKYHI simulations. The SKYHI results are actually for the 16th model level from the bottom, which has a pressure of 103 mb.

ridional circulation by the upper boundary condition and the omission of exotic physical effects in the SKYHI treatment of radiative transfer that may become important in the upper mesosphere (e.g., Mlynczak and Solomon 1993). Work is now in progress on a version of SKYHI that will include considerable vertical resolution in the lower thermosphere as well as an attempt at a more complete treatment of radiative processes. The simulation of the observed summer mesopause temperature in such a GCM would then be a rather stringent test of the adequacy of the model gravity wave field.

6. Quadratic eddy quantities

The basic measures of eddy activity and eddy fluxes are summarized in this section. The eddy component will be defined simply as the deviation from the zonal mean. The stationary component is defined here as the long-term (10 year, 2 year, and 1 year for *N*30, *N*45, and *N*90, respectively) mean. The transient component is then the deviation from the long-term monthly mean for each calendar month. This definition is compatible with the definitions of stationary and transient eddies employed in the observational sources SPMSW and Wu et al. (1987), based on eight and four years of data, respectively. The use of different record lengths for the different models and observational datasets leads to some ambiguity in interpreting the stationary/transient decomposition. In particular the datasets with shorter records will tend to assign more of the eddy variance into the stationary component.

a. Eddy kinetic energy

Figure 14 shows the DJF mean eddy kinetic energy per unit mass (EKE) from observations (from SPMSW available only to 100 mb) and the three versions of SKYHI. Figure 15 shows the same comparison but for only the transient EKE. In the troposphere SKYHI captures the EKE peak near the core of the subtropical jet in each hemisphere. The peak value in the simulations increases with resolution. This makes the *N*90 version the most realistic simulation of the SH EKE, but the *N*90 model overestimates the peak EKE in the NH subtropical jet. The tropical upper troposphere has another maximum in EKE in the *N*30 model that has no analog in the observations. Other investigators have noted the same effect in their GCMs (e.g., Manabe and Mahlman 1976; Boville 1991). It is interesting that this model peculiarity is virtually eliminated at *N*90 resolution. [This improvement with resolution is also found in Boville (1991).]

The NH middle atmospheric values in Figs. 14 and 15 may not be too meaningful for the *N*45 and *N*90 models, given the large interannual variability expected. The SH (i.e., summer) values are very interesting, however. Figure 15 shows that the transient EKE in the high-latitude upper stratosphere and mesosphere systematically increases with resolution. This presumably reflects the more energetic gravity wave field in the higher-resolution versions.

Figure 16 shows the total EKE in JJA. Again, an interesting aspect of the tropospheric results is the improvement of the SH simulation with increasing resolution. At *N*30 the maximum in EKE in the SH troposphere is located at unrealistically high latitudes. This discrepancy is significantly reduced in the higher-resolution versions. The unrealistic tropical upper-tropospheric maximum in total EKE in the *N*30 version is seen in JJA as well. Again this problem is virtually absent in the *N*90 simulation. The peak NH tropospheric transient EKE in JJA (not shown) is underestimated by all three versions of SKYHI. This underprediction of summertime transient EKE has also been found in other GCMs (e.g., Manabe and Mahlman 1976). The increase in the JJA high-latitude NH mesospheric EKE with resolution seen in Fig. 16 parallels the SH summer results noted earlier.

b. Eddy fluxes

Figure 17 shows the DJF total eddy northward flux of zonal momentum per unit mass from the model and from observations. Note that the observations above 100 mb are taken from Wu et al. (1987) and reflect only the component associated with the geostrophic wind. The tropospheric momentum fluxes have an interesting dependence on resolution. In both hemispheres the poleward flux in the subtropical jet regions

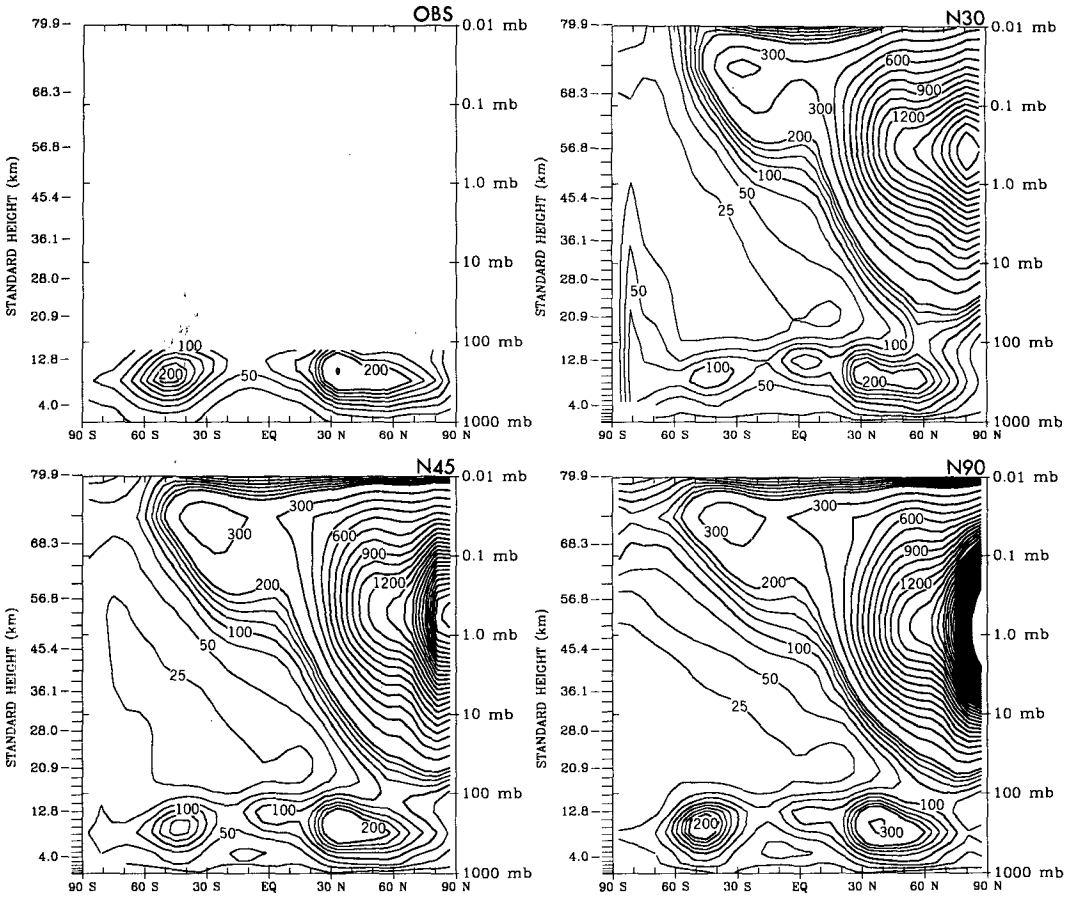

FIG. 14. Total eddy kinetic energy per unit mass in the DJF period. Results for observations and for the *N*30, *N*45, and *N*90 SKYHI simulations. The contour values are 25, 50, 75, 100, 200, 300 . . . $m^2 s^{-2}$.

increases with resolution. In the SH this flux is greatly underestimated by the *N*30 model and is near the observed value in the *N*90 simulation. In the NH, the flux is rather realistic at *N*30 and increases to values ~30% larger than observed by *N*90. This resolution dependence of the momentum fluxes is reflected in the surface flow simulations examined in section 4a (stronger poleward eddy momentum transports need to be balanced by increased drag on the midlatitude surface westerlies). The large peak (>70 $m^2 s^{-2}$) seen in the midlatitude momentum flux in the *N*45 and *N*90 SKYHI results is closely paralleled by Boville's (1991) results with his T63 spectral model (see his Fig. 6).

The model results in the stratosphere display a strong peak around 60°N and 0.6 mb. This has an apparent counterpart in observations, but in SKYHI the maximum magnitude of the flux apparently is overestimated (by a factor of ~2–3). The present model results are strikingly similar to those of Boville (1991; see his Fig. 6), who finds a peak value of about 500 $m^2 s^{-2}$ at T31 resolution and 800 $m^2 s^{-2}$ in his highest-resolution model (T63). Note that the large upper-stratospheric values in these GCMs are unrealistic when compared with any of the Wu et al. (1987), Randel (1992), or Hamilton (1982a) observational climatologies of eddy momentum flux. The observational comparison in Fig. 17 above 100 mb is complicated by the fact that the model results are for the full velocity, while the Wu et al. climatology uses geostrophic winds. Boville (1987) examined this issue for NH winter and found that use of the geostrophic approximation leads to an overestimate of the peak poleward momentum fluxes by as much as 40% in the upper stratosphere. This makes the effective discrepancy between observations and model in Fig. 17 even larger.

Figure 18 shows the same DJF comparison but for the northward flux of temperature. The overall simulation in the heat flux in the winter troposphere and lower stratosphere appears reasonably good, but the model greatly overpredicts the fluxes at high latitudes above about the 30-mb level. Again, if the very small sample is to be trusted, this unrealistically large stratospheric heat flux is most evident at *N*90 resolution.

Figure 19 displays the eddy northward flux of zonal momentum per unit mass for the JJA season. In the

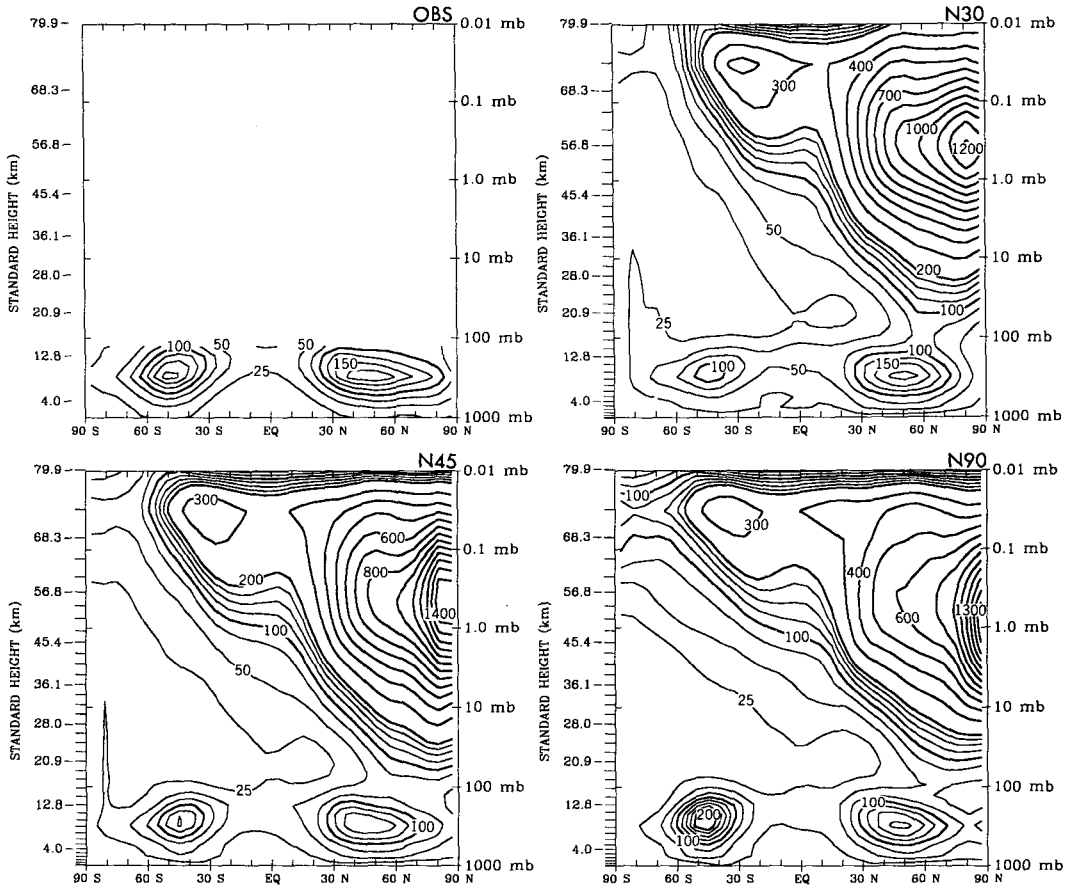

FIG. 15. As in Fig. 14 but for the transient eddy kinetic energy per unit mass.

SKYHI troposphere the momentum fluxes in SH winter display an even stronger dependence on resolution than in the NH winter. The observations indicate a region of poleward momentum flux between about 10° and 50°S, reaching as much as 40 $m^2 s^{-2}$ near the tropopause at 30°S. At *N*30 resolution both the extent and strength of this area of poleward flux is very poorly simulated. This is yet another indication of the very inadequate representation of the SH tropospheric meteorology at *N*30 resolution. The tropospheric momentum flux simulation is considerably improved at *N*45 and *N*90 resolutions.

Given the very strong dependence of the JJA tropospheric eddy flux on resolution, it is perhaps surprising to see the relative insensitivity of the lower-stratospheric results in Fig. 19. It appears that the *N*30 model may indeed do a poor job at simulating many aspects of the tropospheric eddies, but that the large-scale eddies that are important in the lower stratosphere may not be so badly represented. The insensitivity of stratospheric eddy fluxes to resolution is also apparent in the JJA eddy temperature fluxes for the three SKYHI versions (not shown).

c. *Eliassen–Palm flux divergence and net radiative heating*

The EP flux divergence provides a convenient measure of the net eddy forcing of the mean flow. As part of the present study, the EP flux divergence [normalized as a zonal force per unit mass; see Andrews et al. (1983)] was computed from daily snapshots of the integrations and then again from the long-term monthly mean history files. The mean of these instantaneous values is the present estimate of the total zonal force per unit mass (ZF), while the analysis of the long-term mean history files yields the stationary component of ZF. Unfortunately, there are no very appropriate observational climatologies for comparison. Randel (1992) does give monthly estimates of ZF up to 1 mb, but these were obtained by neglecting the terms involving vertical velocity.

The upper left panel of Fig. 20 shows the total *N*30 ZF for the DJF period. The most obvious features here are the strong easterly mean flow driving in the winter mesosphere and a corresponding westerly driving in the summer mesosphere. These are largely the result of

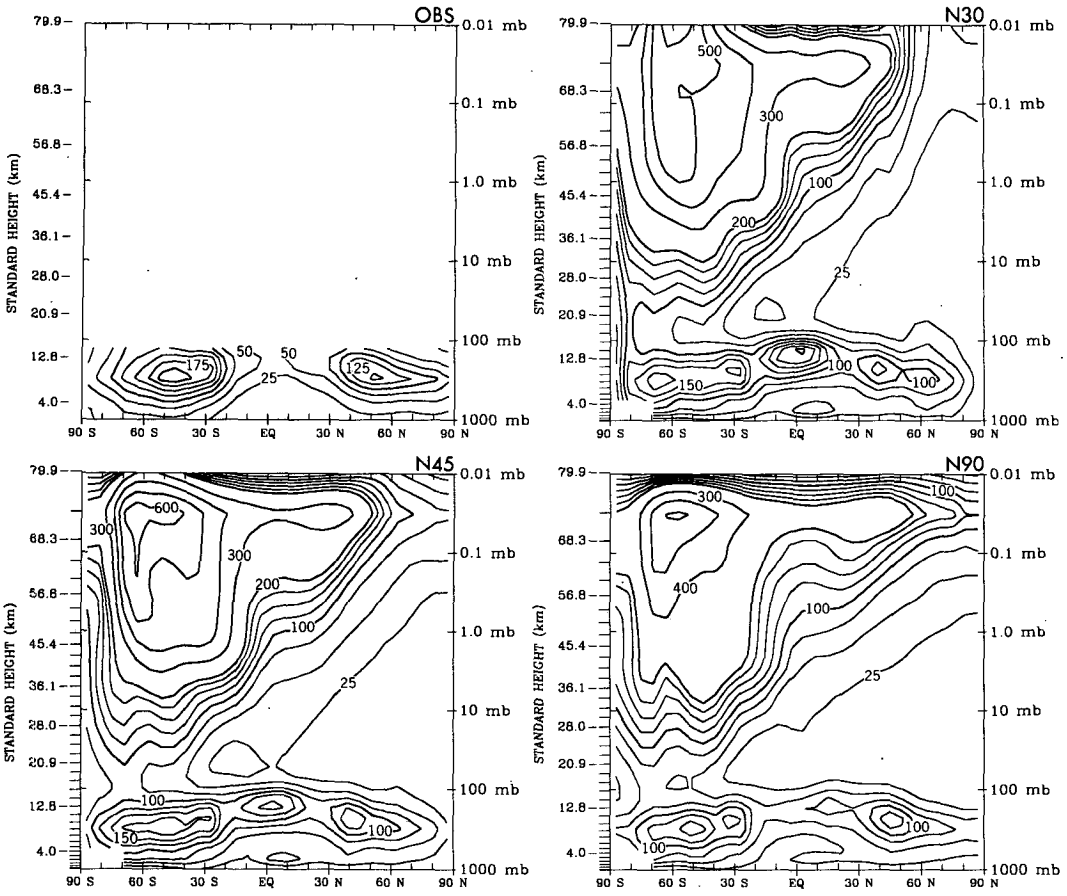

FIG. 16. As in Fig. 14 but for the JJA period.

vertical momentum flux convergence associated with gravity waves. The upper right-hand panel shows the stationary component computed from 10 years of the *N*30 integration. As expected, this is very small in the summer hemisphere middle atmosphere (and in the Tropics). The stationary component accounts for most (but not all) the ZF in the NH stratosphere but is less important than the transient component in the NH upper mesosphere. The lower left panel shows the difference in the ZF in the *N*45 model when compared with the *N*30 climatology. The lower right-hand panel shows the difference in ZF between the *N*90 and *N*30 runs. The winter hemisphere results for *N*45 and *N*90 may not be significant, given the limited data available (it is noteworthy in this regard how noisy the *N*90 − *N*30 difference field is in the NH). In the summer hemisphere the results are presumably fairly repeatable from year to year, and the differences indicated in Fig. 20 are likely significant. The results show that the westerly drag on the summertime mesospheric jet increases systematically with resolution, particularly at high latitudes. This increasing drag (which is also accompanied by the increase in transient EKE at high summer latitudes) is the cause of the improvement with resolution in the simulation of the zonal-mean wind and temperature structure in the summer mesosphere (see section 5).

Figure 21 shows the same quantities as Fig. 20 but for the JJA period. The NH summer mesosphere has a similar dependence of ZF on resolution as seen earlier in the SH summer. In the winter hemisphere the results are very interesting. As resolution is increased the easterly ZF in the SH upper mesosphere increases (except at the top level in the *N*90 version). This change is quite large, particularly in the middle mesosphere (near the third and fourth model levels from the top). The cold bias in the polar upper stratosphere also improves dramatically with increasing resolution (Fig. 12). Haynes et al. (1991) note that the effects of an isolated region of ZF can be felt on the zonal-mean circulation well below the region itself. This is particularly the case when the radiative relaxation timescale for the mean state is long. Since the simulated temperatures in the SH winter upper stratosphere are so cold, the effective radiative damping here should be relatively weak. Thus, the improvement with resolution in the mean

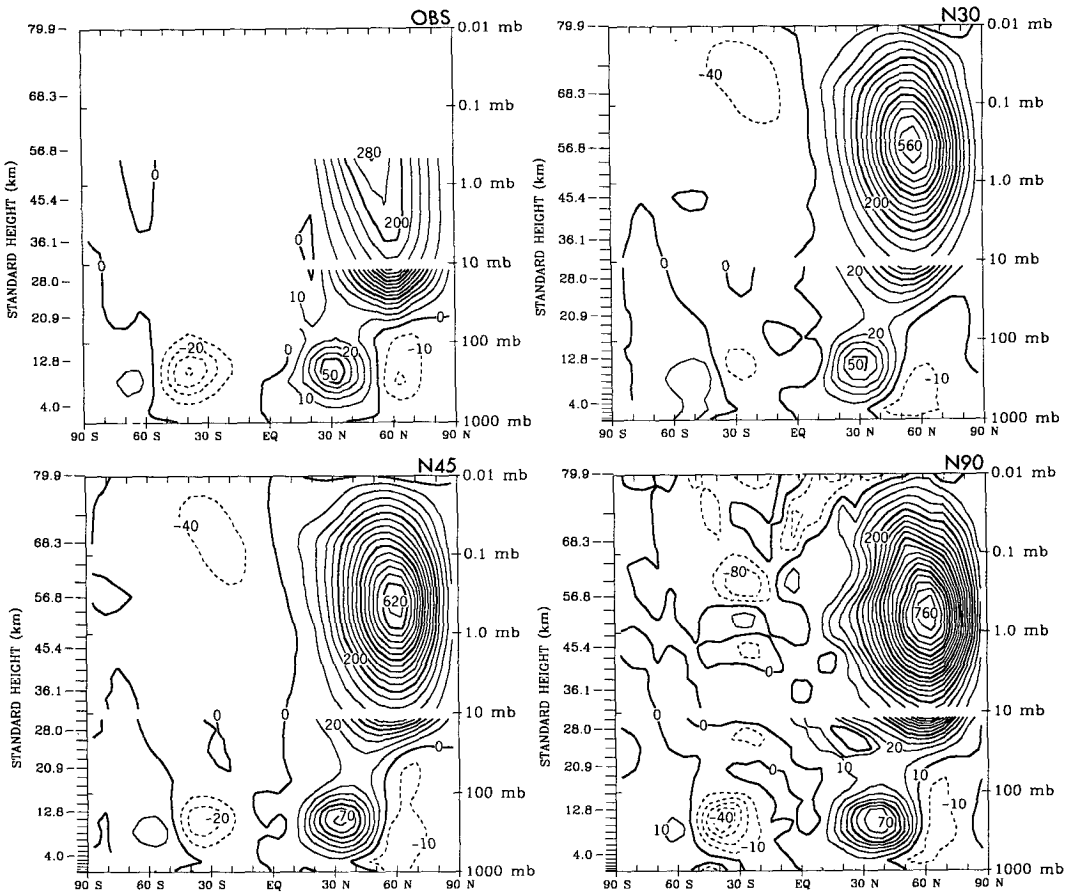

FIG. 17. The northward flux of zonal momentum per unit mass by eddies for the DJF period. Results for observations and for the *N*30, *N*45, and *N*90 SKYHI simulations. The contour interval below 10 mb is 10 $m^2 s^{-2}$, and above 10 mb it is 40 $m^2 s^{-2}$; heavy contours are used every 200 $m^2 s^{-2}$.

stratospheric simulation may largely reflect the increasing mesospheric gravity wave drag resolved by the model. The dependence of the circulation response on a radiative damping timescale may help explain why the deficiencies in the resolved gravity wave drag in the summer hemisphere (apparent in the polar mesopause temperature simulation) apparently have much less drastic effects on the summer upper-stratosphere temperature.

It is interesting to compare the results in Fig. 21 to the calculations of Shine (1989). He attempted to deduce the distribution of eddy ZF that could account for the observed zonal-mean temperature structure of the atmosphere. Shine found that in the SH winter he required an easterly ZF peaking in midlatitudes and around 0.1 mb of about 60 m s^{-1} d^{-1}. Figure 21 shows clearly that the *N*30 model falls well short of reaching this value of ZF at the 0.1-mb level, but that a significant improvement is evident at *N*90 resolution. It is reasonable to expect that the mesospheric ZF would continue to increase if the model resolution were to be further improved, and that this would reduce the polar upper-stratospheric cold bias.

Figure 22 shows the long-term mean zonally-averaged net radiative heating rates for DJF and JJA for each of the model resolutions. These heating rates can be compared with those obtained through radiative calculations using observed temperatures by Rosenfeld et al. (1987) or Shine (1989), although both these references present only January and July values. The overall distribution of net heating in the DJF SKYHI model results is similar to that obtained in the earlier calculations. In particular, the peak cooling rate at the winter pole in DJF in SKYHI ($\sim$9–10 K d^{-1}) agrees well with that in the January results of Shine and Rosenfeld et al. The heating rate structure in the SKYHI SH winter deviates rather obviously from the earlier calculations (reflecting the fact that the simulated temperature structure is much more realistic in DJF than in JJA). At all three model resolutions the JJA cooling rate reaches a maximum at the top level in the high latitude SH, whereas the calculations of Rosenfeld et

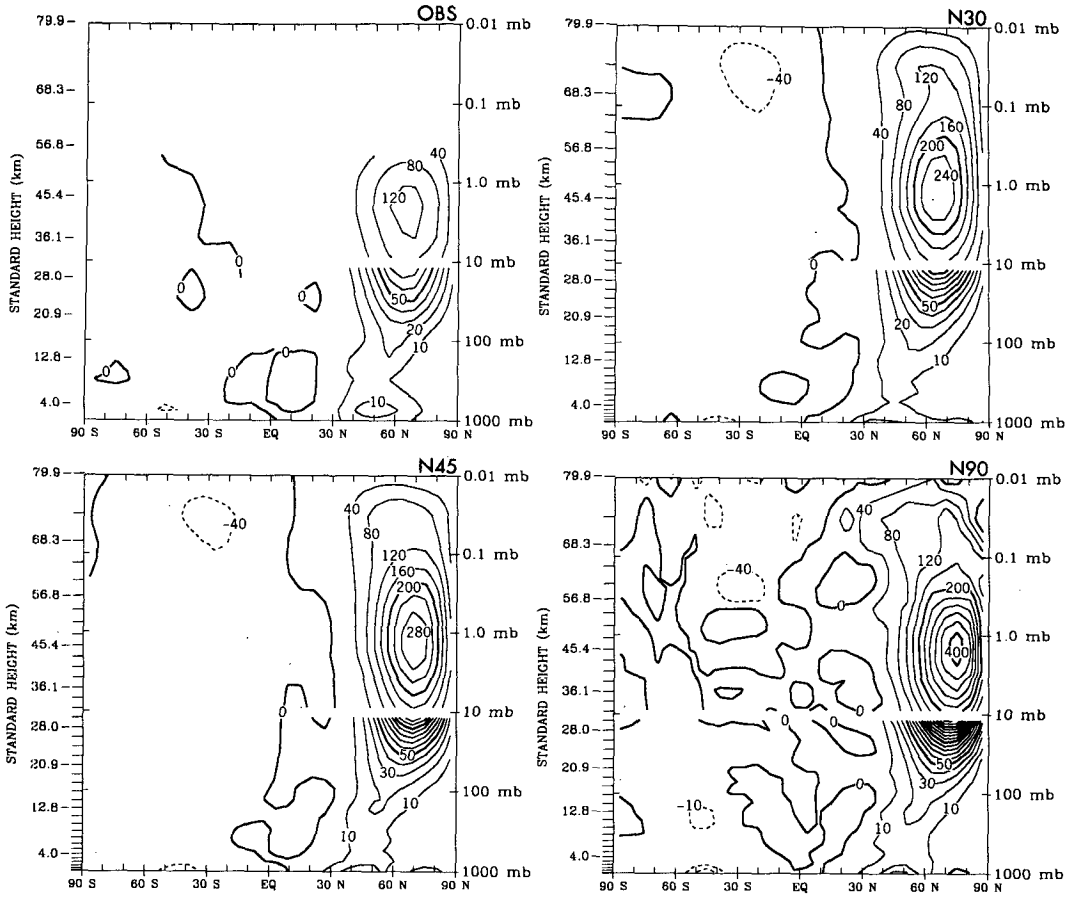

FIG. 18. The northward flux of temperature by eddies for the DJF period. Results for observations and for the *N*30, *N*45, and *N*90 SKYHI simulations. The contour interval below 10 mb is 10°C m s^{-1}, and above 10 mb it is 40; heavy contours are used every 200°C m s^{-1}.

al. and Shine both suggest that the peak cooling (of about 12 K d^{-1}) should occur in the lower mesosphere.

The lower- and middle-stratospheric results from SKYHI in both seasons tend to be closer to those of Rosenfeld et al. than to those of Shine. In particular, Shine finds net cooling at all latitudes around 10 mb and only a very small region of positive heating at levels below 10 mb, while the present results show that in SKYHI there is net heating in the Tropics and most of the summer hemisphere, in accord with the Rosenfeld et al. calculations.

The SKYHI heating rates show the largest sensitivity to horizontal resolution at the top model level. The net cooling, which is evident in the Tropics in *N*30, is much intensified at *N*45 and *N*90 resolution (in both DJF and JJA). This reflects changes in the temperature at the top model (see Figs. 10 and 12). The circulation induced by the eddy ZF brings warm air to the upper mesosphere and carries away cold air to lower levels. At the top model level this process is clearly strong enough to significantly affect the global-average heat balance. As noted earlier, the mesospheric ZF driving the circulation intensifies with increasing model resolution (in both hemispheres) and the global-mean heating at the top level displays the same sensitivity to model resolution.

7. Middle atmospheric stationary waves

In this section a detailed comparison will be made between the NH winter stationary wave field seen in the time mean of the SKYHI integrations and in comparable observations. The main focus is on the *N*30 simulation, for which multiyear means are available. The left-hand panels in Fig. 23 show the NH 10-mb, 30-mb, and 50-mb DJF mean geopotential heights averaged over 25 years of the *N*30 integration. The corresponding right-hand panels show the same quantities computed from the subjective NH analyses produced at the Free University of Berlin averaged over comparably long records (34 years at 50 and 30 mb, and 17 years at 10 mb). The same basic features of the wave field are apparent in both model and observations.

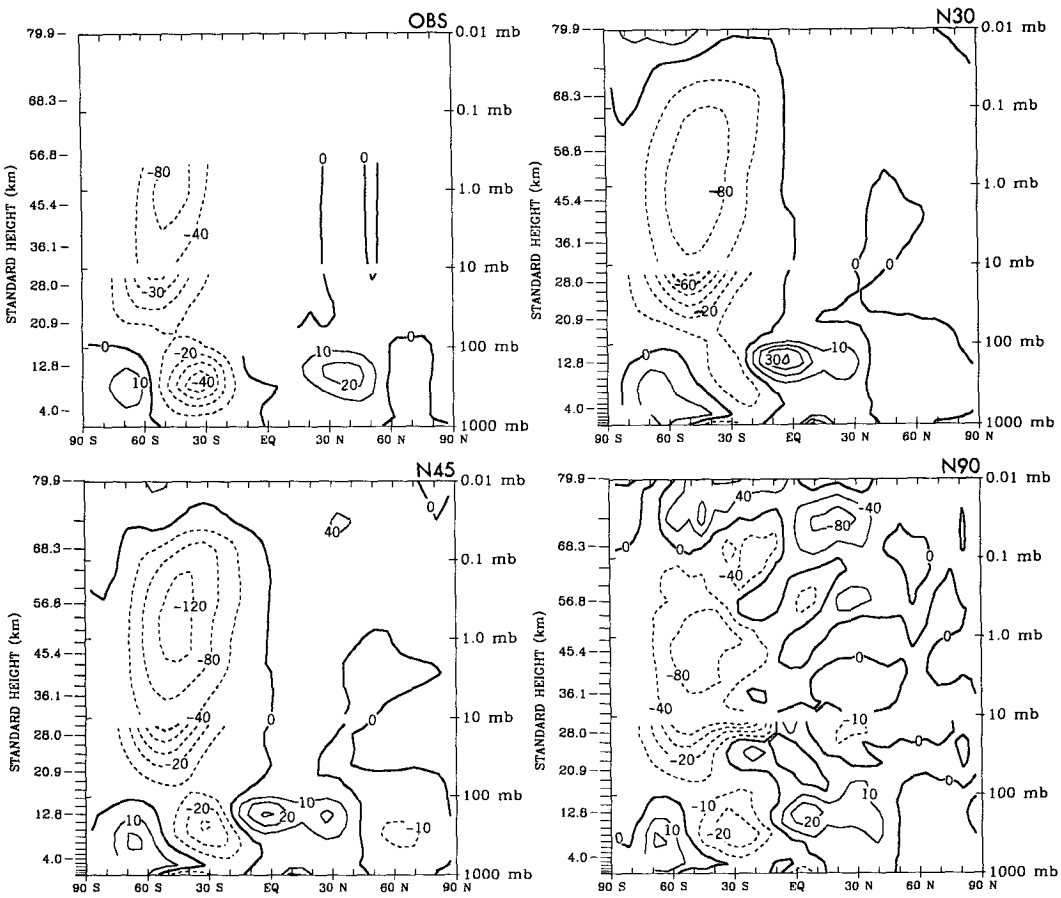

FIG. 19. As in Fig. 17 but for the JJA period.

The combination of zonal wave 1 and 2 components result in an elongation of the polar vortex roughly along the 90°E–90°W axis and a displacement of the vortex center off the pole roughly along the Greenwich meridian. The phase of the whole pattern tilts westward with height, so that in the observations the Aleutian high is centered near 150°W at 50 mb and near 175°E at 10 mb. The *N*30 simulated stationary wave phase tilt is even more pronounced, with the Aleutian high at 10 mb centered near 160°E. The magnitude of the geopotential gradients seen at 50 and 30 mb in the model agree quite well with those observed. However, a comparison of the time-mean geopotential maps at 10 mb shows signs of the model bias noted earlier, that is, a tendency to have a polar vortex that is unrealistically confined to high latitudes. The geopotential gradients in the model vortex are clearly stronger than those indicated in the observations. Looking at the 10-mb results in Fig. 23, one appreciates how the model might overestimate the eddy momentum transport at high latitudes. The overall shape of the model-simulated pattern agrees reasonably well with observations, implying a roughly comparable meridional excursion for air parcels following the time-mean flow. However, given the faster flow in the model vortex, the computed poleward momentum transport will be stronger for the simulation than for observations.

The long series of detailed NH analyses from the Free University of Berlin unfortunately extend only up to 10 mb. Comparisons with satellite data in the upper stratosphere and mesosphere are also possible, of course. The right-hand panels of Fig. 24 show the 25-year January mean amplitude and phase of the zonal wavenumber 1 component of the temperature in the *N*30 integration. This is compared on the left-hand side to observations of the same quantity taken from Barnett and Corney (1985b; hereafter BC), based principally on about 5 years of satellite radiometer data. Figure 25 shows the same comparison for the zonal wavenumber 2 component. The phase convention in each case is that of BC; that is, the temperature as a function of longitude λ is given as

$$T(\lambda) = T_0 + T_1 \cos(\lambda - \phi_1) + T_2 \cos(2\lambda - \phi_2) + \text{higher zonal harmonics},$$

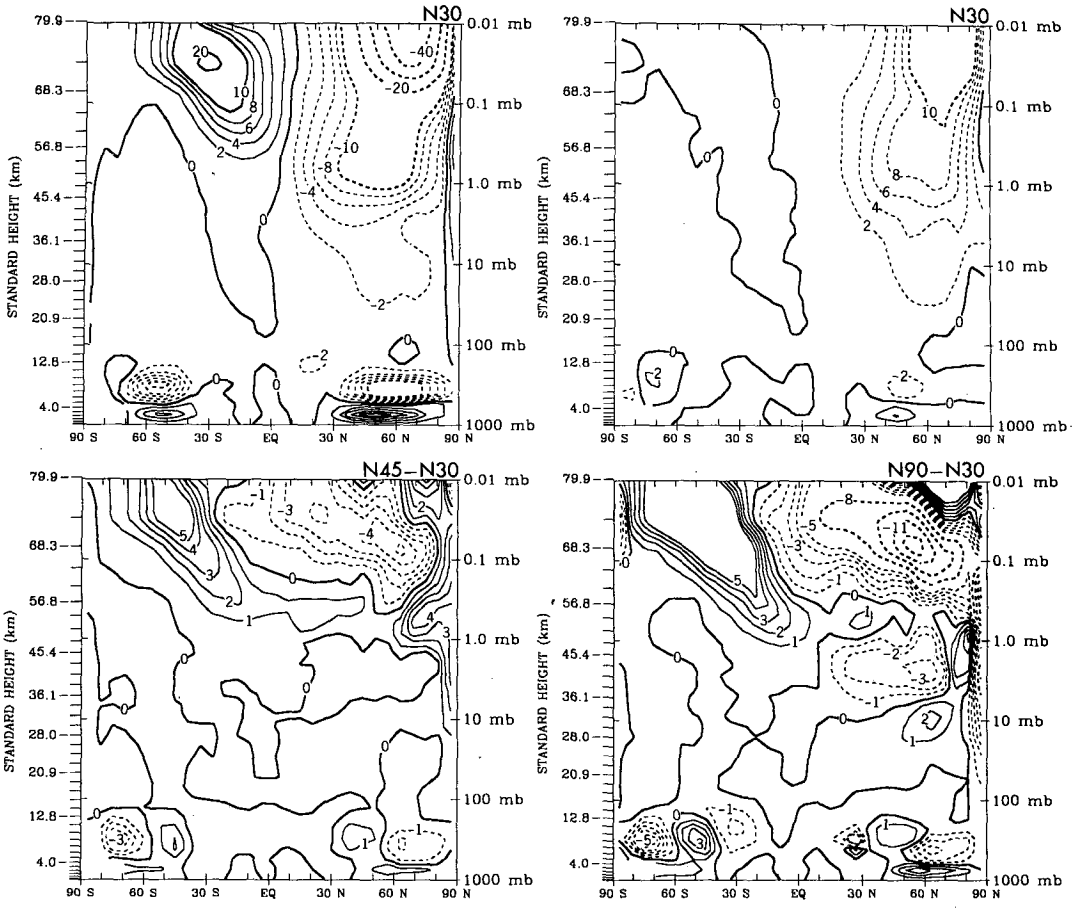

FIG. 20. The top left panel shows the total zonal force per unit mass resulting from the eddy fields in the *N*30 model for the DJF period. The top right panel shows the same quantity but calculated only for the stationary eddies. For both panels the contour values are 0, 2, 4, 6, 8, 10, 20, 30 . . . m s^{-1} d^{-1}, and dashed contours denote easterly mean flow forcing. The lower left panel shows the difference in the total zonal force per unit mass between the *N*45 and *N*30 models. The lower right panel shows the same quantity but now for the difference between the *N*90 and *N*30 simulations. In both panels the contour values are 0, 1, 2, 3, 4, 5, 8, 11, 14 . . . m s^{-1} d^{-1}, and dashed contours show regions where the eddy driving is more easterly in the higher-resolution model.

where λ is measured in degrees east of Greenwich and T_0, T_1, T_2, ϕ_1, ϕ_2 are only functions of pressure and latitude. The phases ϕ_1 and ϕ_2 are quite variable in regions where the corresponding amplitudes T_1 and T_2 are small, particularly in the observations. Figures 24 and 25 follow BC in not plotting the phases wherever the amplitudes fall below specified thresholds.

There is a very rough agreement between the observations and model results for wave 1 when compared in this way. In particular, the vertical and meridional phase propagation is quite similar in the model and in BC, at least up to 0.1 mb (at higher levels the model stationary wave has much less vertical phase propagation than indicated in the observations). The agreement for the amplitude structure of wave 1 is not as good, however. The observations display an isolated maximum in the high-latitude lower stratosphere that does not have a counterpart in the *N*30 results shown in Fig. 24b. The satellite-based observations of BC may not be particularly reliable at these relatively low levels, however. Van Loon et al. (1973) present wave 1 temperature amplitudes in several individual Januarys at 65°N up to 10 mb based on radiosonde data (see their Fig. 10). These results show little hint of the lower-stratospheric maximum found by BC.

The peak amplitudes for wave 1 in the middle stratosphere are roughly comparable (~10°C in BC vs ~14°C in the model), but the SKYHI results show a second amplitude maximum in the mesosphere that is not found in BC. Given the long SKYHI record that is used to construct Fig. 24b, this mesospheric maximum (associated with a nearly barotropic phase structure; see Fig. 24d) is presumably a robust feature of the stationary wave field in the model.

The results for wavenumber 2 shown in Fig. 25 reveal reasonably good agreement between SKYHI and

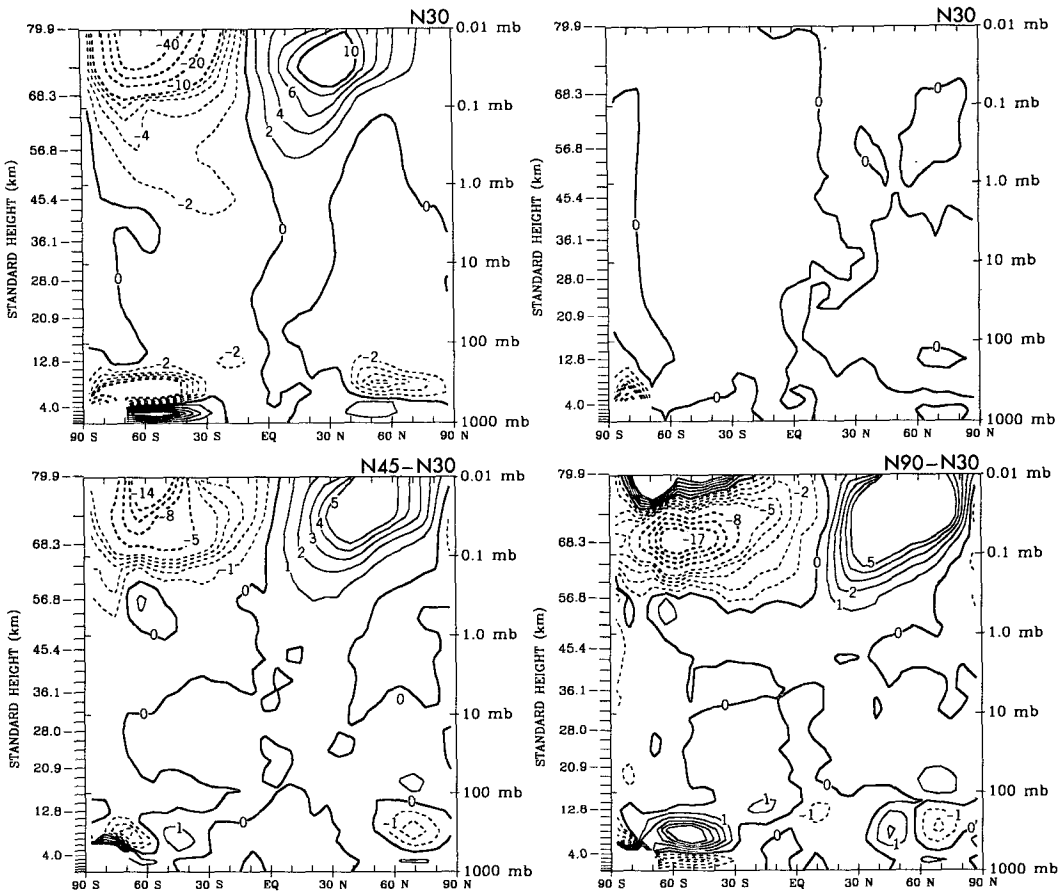

FIG. 21. As in Fig. 20 but for the JJA period.

BC in the lower stratosphere. As expected from basic considerations (Charney and Drazin 1961) the stationary wave 2 perturbation penetrates less deeply into the stratosphere than the corresponding wave 1. The model displays a second large maximum in wavenumber 2 amplitude in the mesosphere, which is not apparent in BC. The wave 2 perturbation in the *N*30 mesosphere has almost no vertical phase propagation (Fig. 25d).

The presence of the (apparently spurious) nearly barotropic wave 1 and 2 stationary waves in the SKYHI mesosphere may possibly indicate problems associated with the upper boundary condition. It will be interesting to examine the mesospheric stationary waves in a version of SKYHI that includes a well-resolved lower thermosphere. The strength of the mesospheric stationary waves in the model may also indicate a deficiency in the effective mechanical dissipation of large-scale waves. Perhaps an even higher-resolution model with a more complete gravity wave spectrum would avoid this problem.

The January mean zonal wave 1 and 2 temperature harmonics were also examined in the *N*90 SKYHI integration (not shown). The *N*90 analysis employed only a single January, and so the results are not strictly comparable to those in the long-term mean of the *N*30 data. Despite this fact, however, the *N*90 results turn out to be qualitatively similar to those obtained for *N*30. In particular the presence of a distinct mesospheric amplitude maximum is apparent for both wave 1 and wave 2.

8. Circulation of the tropical middle atmosphere

Some of the most intriguing aspects of the observed middle-atmospheric circulation occur at low latitudes. Modeling the quasi-biennial oscillation (QBO) and semiannual oscillation (SAO) remain important challenges for GCMs. The tropical stratospheric circulation revealed in an earlier *N*30 SKYHI integration was discussed by Hamilton and Mahlman (1988; hereafter HM88). They showed that the model produced a stratopause SAO with approximately realistic amplitude, phase, and meridional and vertical extent. Both the easterly and westerly phases were somewhat weaker than observed; in particular the very strong westerly shears reported from observations by Hitchmann and

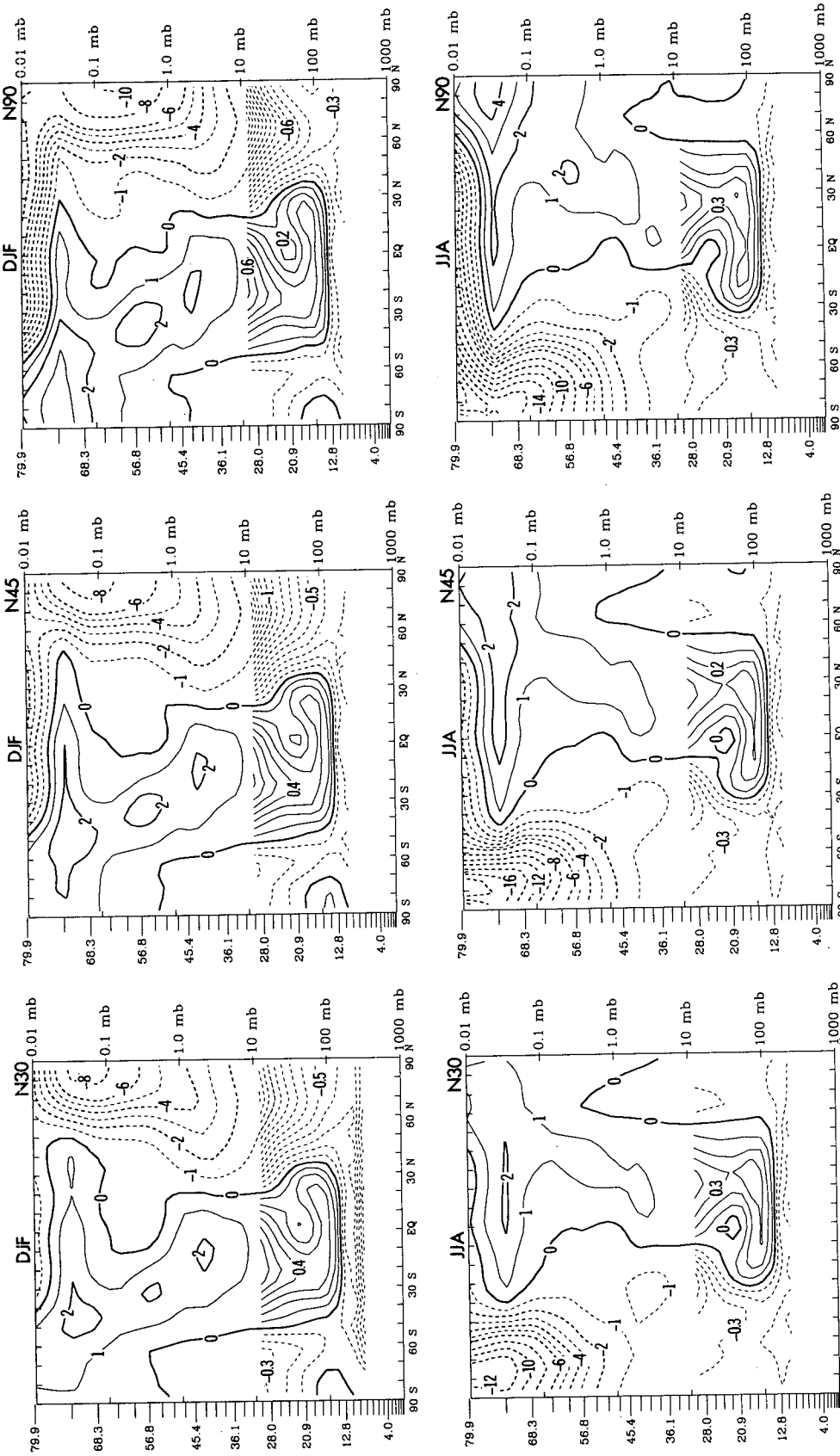

FIG. 22. Climatological net radiative heating rates for the three SKYHI resolutions in both DJF (top row) and JJA (bottom row). The contour interval below 10 mb is 0.1 K d^{-1}, and above 10 mb it is 1 K d^{-1}. The 0 contour is emphasized, and dashed contours denote areas of net cooling.

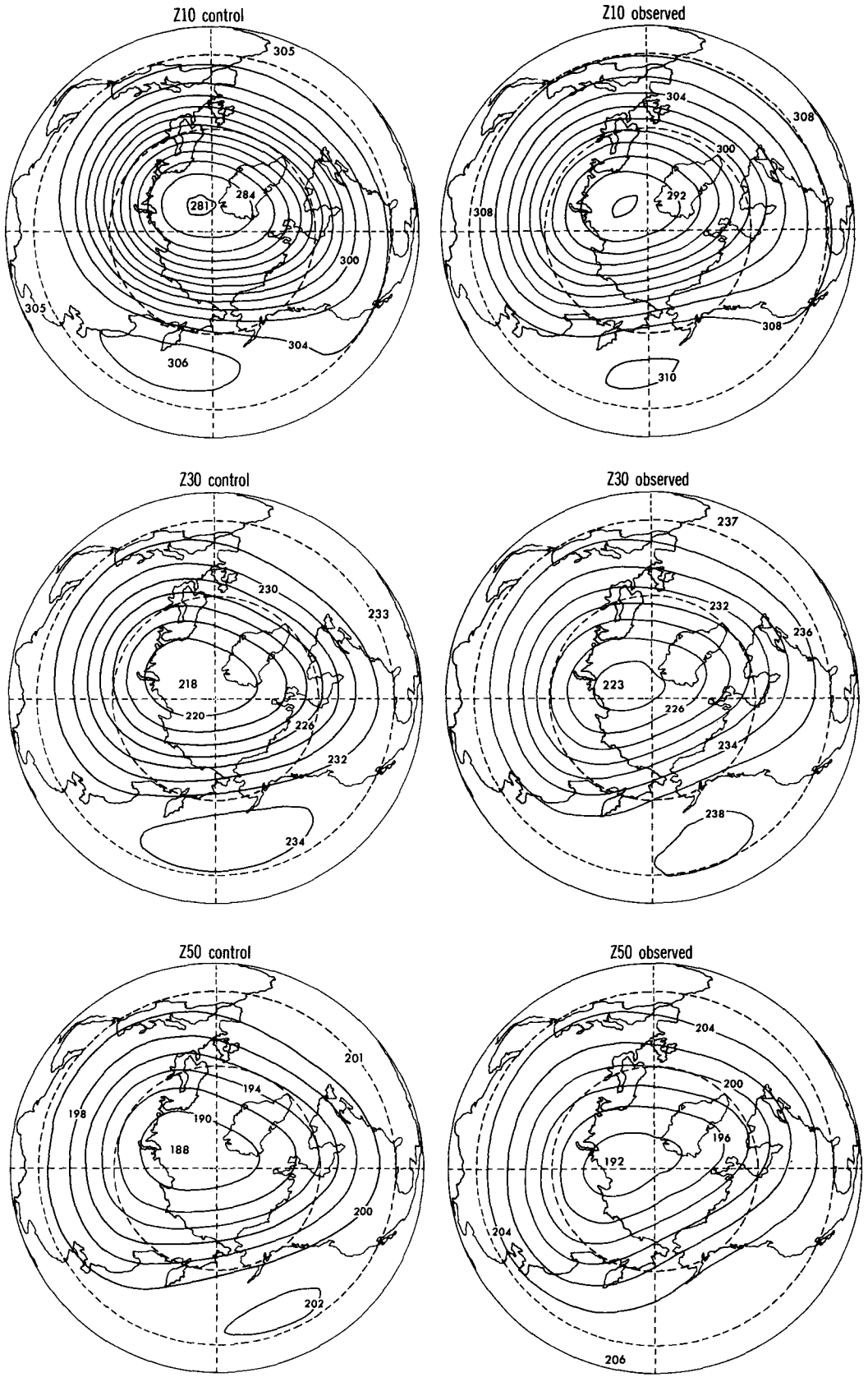

FIG. 23. The long-term mean DJF geopotential heights at 10 mb (top), 30 mb (middle), and 50 mb (bottom) from the *N*30 SKYHI simulation (left) and observations (right). The contour labels are in hundreds of meters, and the contour interval is 200 m. The dashed circles show 30° and 60°N.

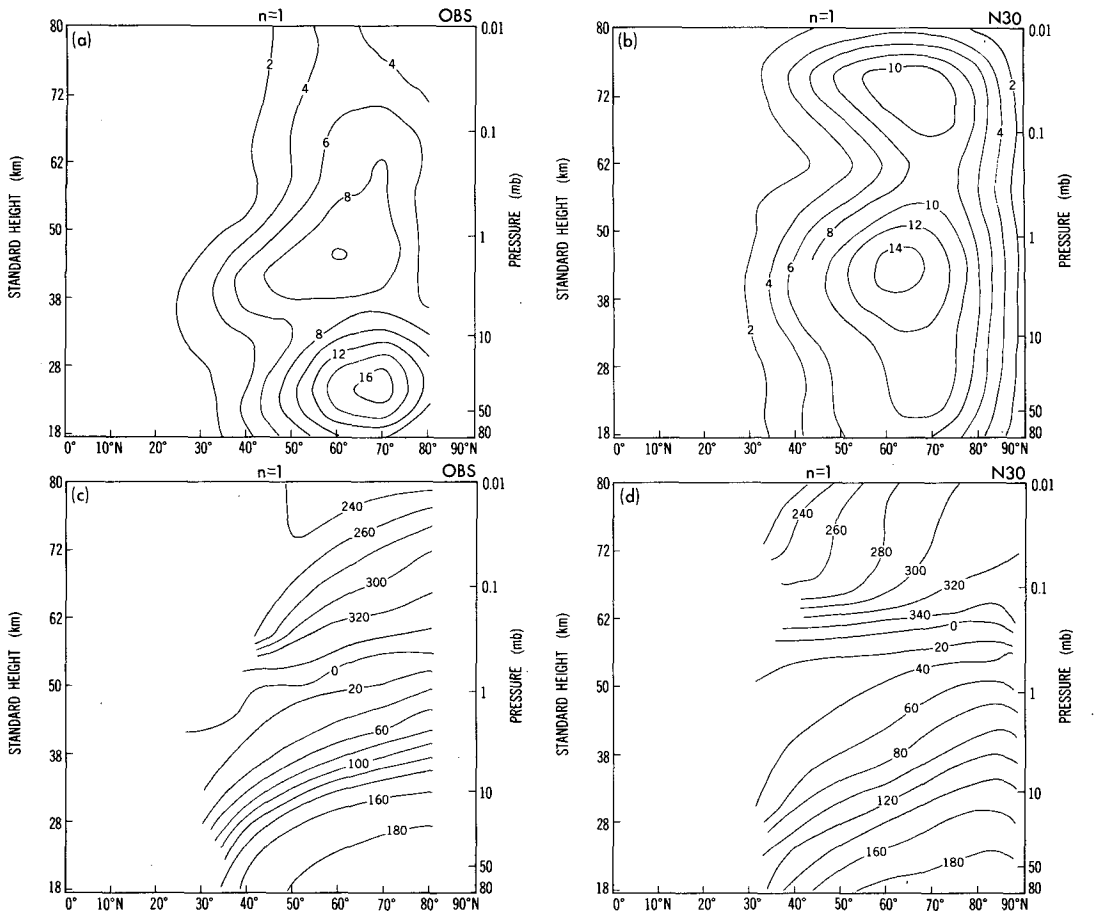

FIG. 24. The amplitude (top) and phase (bottom) of the long-term mean zonal wavenumber 1 component of temperature in January. The amplitude is labeled in degrees Celsius, and the phase in degrees of longitude. No phases are plotted for the region where the amplitude drops below 2°C. Results from observations (left) and *N*30 SKYHI simulation (right).

Leovy (1986) were not reproduced in the simulation. The simulated easterly phase was also somewhat weaker than observed, and the observed equatorial easterly core is more localized in height than that found in the model. In addition to the familiar stratopause SAO, rocket and radar observations (Hirota 1978; Hamilton 1982b; Paolo and Avery 1993) show that there is a second peak in the amplitude of the semiannual harmonic of the zonal wind near the mesopause. This mesopause SAO has an amplitude of $\sim$20 m s^{-1} and is roughly 180° out of phase with the stratopause SAO. HM88 found some evidence for a mesopause SAO with the correct phase but unrealistically small amplitude at the top level of the *N*30 SKYHI model. Comparisons with observations are complicated by the fact that the model domain terminates at about 80 km (i.e., below the peak of the observed oscillation).

The analysis of HM88 exposed the absence of anything approaching a realistic QBO in the tropical lower stratosphere. This is a deficiency that is apparently shared by all extant comprehensive GCMs (e.g., Boville and Randel 1992; Hamilton and Yuan 1992), although Cariolle et al. (1993) reported a very weak ($\sim \pm 4$ m s^{-1}) near-biennial signal in the equatorial middle-stratospheric winds in three spectral GCMs. In this section the equatorial mean flow evolution in SKYHI will be examined in the long control integration with the current version of the *N*30 model and in the brief *N*90 integration available.

a. Semiannual oscillation

Figure 26 shows the time–height section of the annual march of the equatorial zonally averaged zonal wind computed using data from 10 years from the *N*30 integration. The basic features of the stratopause SAO are evident. The oscillation peaks near 1 mb, where easterlies (westerlies) are maximum in January and July (April and October). There is also a clear downward phase propagation similar to that observed. There are some significant differences near the stratopause between the present *N*30 simulation and that reported

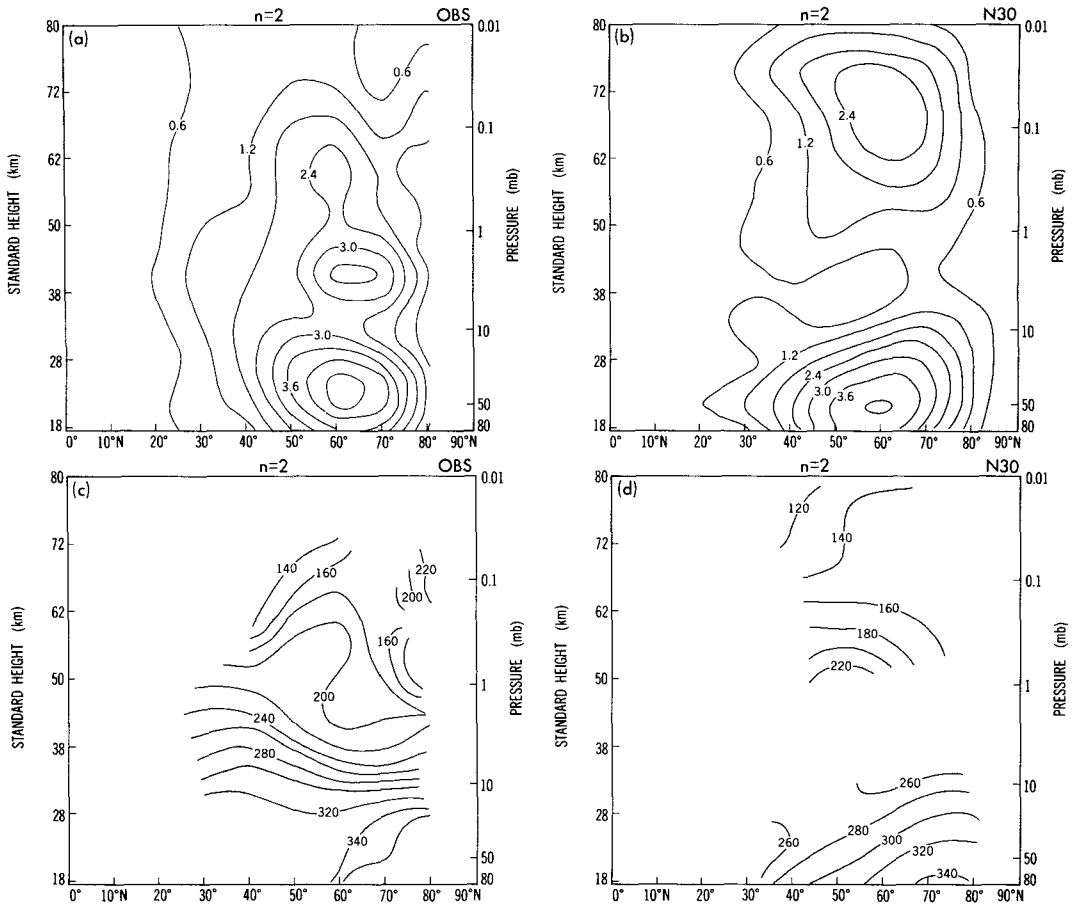

FIG. 25. As in Fig. 24 but for zonal wavenumber 2. No phases are plotted for the region where the amplitude drops below 1.2°C.

in HM88 (see Fig. 6 of HM88). The simulated easterly phase in the current *N*30 model is more realistic than in HM88, with stronger and more localized easterlies. However, the westerly phase in the present simulation is actually weaker (and hence less realistic) than in HM88. The only plausible reasons for these changes are the correction of the code error in the convective adjustment (section 2g) and the changes in the stratospheric heating rates due to the improved diurnal averaging procedure (section 2e). Other experiments show that changes in the equatorial upper-stratospheric mean winds of the order of 10–20 m s^{-1} can be reasonably attributed to the code error correction. Changing the convection scheme presumably alters the spectrum of the upward propagating waves emerging from the tropical troposphere and hence the mean flow that is forced.

Recently Sassi et al. (1993) have examined the stratopause SAO simulated in a 75-level, T31 spectral model. The basic results for SAO in zonal wind are fairly similar in their model and in the present results. Both models are unable to reproduce the strong westerly shears reported by Hitchmann and Leovy (1986). In general, the results of Sassi et al. more closely resemble the simulated SAO in the present *N*30 SKYHI than the earlier simulation reported by Hamilton and Mahlman (1988).

The present *N*30 simulation near the equatorial mesopause is similar to that found in HM88. There is an unrealistic westerly bias in the annual-mean winds and at least a hint of a semiannual variation roughly out of phase with the SAO at the stratopause (this is seen clearly when the mean and annual harmonic are removed from the seasonal march).

An examination of the seasonal evolution of zonal wind in the last two years of the *N*45 integration (not shown) reveals great similarities with the *N*30 results in Fig. 26 (the westerly bias in the upper mesosphere is slightly reduced in the *N*45 case). A preliminary examination was made of the equatorial mean flow evolution in the present *N*90 experiment (not shown). Of course, the mean flow changes that are seen in this integration will reflect to some extent the relaxation of the flow to a new equilibrium appropriate for the re-

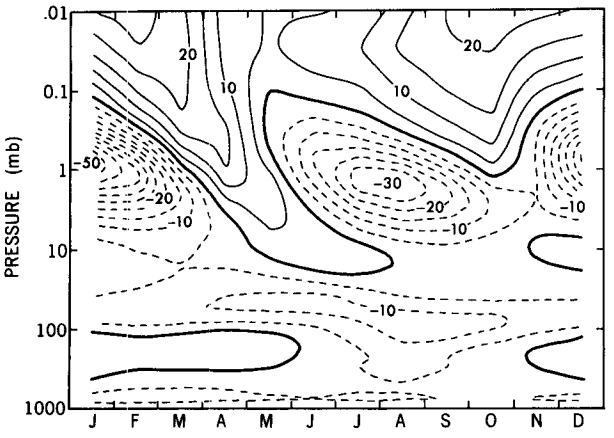

FIG. 26. Time–height section for the long-term mean annual cycle of equatorial zonally averaged zonal wind from the *N*30 SKYHI integration. Contours are based on the 12 monthly means. The contour interval is 5 m s^{-1} and dashed contours denote easterly winds.

vised model. In fact the flow evolution in JJA *1984* is significantly different from the same period in *1983*. The stratopause SAO seen in the last 12 months is fairly realistic. The December–January easterly maximum in *N*90 appears somewhat weaker than in *N*30 and even more localized in height. Whether this difference will be found in succeeding years of the *N*90 integration or whether it merely reflects the nonequilibrium nature of the solution at this point remains to be seen.

In summary, the improvements in model physics from the HM88 results and the increase in horizontal resolution from *N*30 to *N*90 both significantly affect the modeled SAO. Unfortunately, neither of these changes appears to unambiguously improve the SAO simulation.

b. Interannual variability

Figure 27 shows the equatorial zonally averaged zonal wind for 10 years of the *N*30 simulation, with the 10-year mean for each calendar month removed. The remaining wind fluctuations display some consistent features, notably a systematic downward phase propagation. The variability peaks around 1 mb, where it is clearly dominated by relatively high frequencies (periods <1 y). The large anomalies (up to 10 m s^{-1}) can occur in any part of the year (in particular, they are not obviously concentrated in boreal winter, when the extratropical interannual variability is expected to peak).

The variability in the lower and middle stratosphere is weaker and is dominated by rather longer period changes. In fact, there is even a quasi-biennial aspect to the wind evolution below about 5 mb, with general downward phase propagation. This very weak QBO ($\sim \pm 2$ m s^{-1}) shares a number of properties with that found by Cariolle et al. (1993) in their spectral model integrations. In particular, the rather irregular nature of the oscillation in the unfiltered wind data is also evident in the results of Cariolle et al. (compare the 10-mb SKYHI results in the present Fig. 27 with their Fig. 1). In addition, both the oscillation documented here and that in Cariolle et al. (1993) are unrealistically confined near 10 mb and are just barely detectable in the lower stratosphere. The QBO fluctuations in the integrations of Cariolle et al. do have somewhat larger amplitude than those found in the *N*30 SKYHI. It must be emphasized, however, that the amplitudes of the equatorial zonal wind oscillations in any of these models is almost an order of magnitude smaller than that of the real QBO.

9. Conclusions

This paper has examined the long-term mean climatology as simulated by the GFDL SKYHI model run at three different horizontal resolutions. The *N*30 and *N*45 integrations were made with model codes identical except for the horizontal resolution. The *N*90 integration suffered from some changes in model formulation during the run, but for the final 15 months of integration the *N*90 model was unchanged. This final version of the *N*90 code differed from the *N*30 and *N*45 models only in the treatment of the surface heat balance. Some aspects of the SKYHI model are significantly different from most other comparable stratospheric GCMs currently in use (notably the finite-difference numerics and the use of unsmoothed topography). Some aspects of the model physics are extremely simple (notably the use of fixed cloud amounts), but much effort has been expended to ensure that the radiative heating rates in the middle atmosphere are computed accurately. The results presented here should provide a hitherto unavailable context for interpreting the nearly 20 published

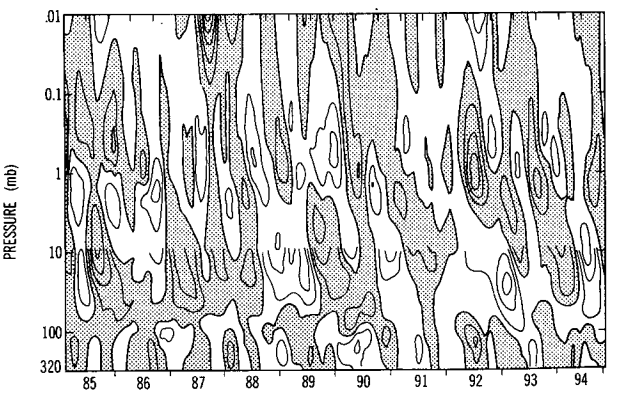

FIG. 27. Ten years of the anomaly in the equatorial zonally averaged zonal wind from the *N*30 SKYHI integration. The period considered is February *1985* through January *1995*. The anomaly is defined as the difference between a particular monthly mean and the 10-year mean for the calendar month. The contour interval is 1 m s^{-1} below 10 mb and 3 m s^{-1} above 10 mb. Shading denotes winds that are anomalously westerly.

papers that have dealt with specific aspects of the middle atmosphere in the SKYHI model. In addition, however, the present model results raise a number of interesting questions about GCMs in general and about the particular challenges of numerical simulation of the middle atmosphere.

Perhaps the most basic quantity in a climate simulation is the global-mean tropospheric temperature. It is apparent that the SKYHI model as now formulated has a pronounced tropospheric cold bias, despite the imposition of realistic sea surface temperatures. The explanation for this problem presumably lies in the distribution of radiative absorbers specified (notably the cloud fields), which can obviously have a large impact on the radiative balance of the entire troposphere. Possible misrepresentation of the radiative heating may also affect the land–sea heating contrast, and it is interesting to speculate on whether this could significantly affect the simulation of monsoon circulations. Certainly it is apparent that the SKYHI model has some difficulty in simulating realistic tropical monsoon rainfall (and that in general the model precipitation simulation is less realistic in summer than in winter).

Despite these possible difficulties in accurately simulating the radiative driving of the lower atmosphere, many of the tropospheric circulation features are reasonably well reproduced by the model. The surface zonal winds (and SLP gradients) in midlatitudes display the sort of sensitivity to model resolution that has been documented in other GCMs without parameterized gravity wave drag. The net result is that the NH SLP distribution is well simulated at *N*30 resolution, while the SH SLP is best represented by the *N*90 model. By contrast, the sensitivity of upper-tropospheric flow to the resolution employed does not appear to be serious, and reasonably good simulations of the time-mean flow are obtained with each of the *N*30, *N*45, or *N*90 versions. This leads to a possible prescription for producing a realistic tropospheric circulation: run the model at high (*N*90) resolution and add a topographic wave drag that acts principally in the lower troposphere. Since this should have little effect in the SH (where there is little topographic relief) the good *N*90 simulation described in section 4a would be preserved, while the drag would reduce the excessive surface westerlies seen in the present *N*90 simulation without affecting the upper-tropospheric flow too much. It remains to be shown that such a scheme would actually work well (as noted earlier, most existing gravity wave drag parameterizations impose the drag mainly at upper-tropospheric levels or distribute it throughout the troposphere). Even if this drag parameterization could be tuned to yield a good simulation of the zonal-mean flow, there remains the question of whether the parameterization represents real atmospheric effects. It is noteworthy that the tropospheric eddy momentum transports in the present *N*90 model are larger than those indicated in the European Centre for Medium-Range Weather Forecasts (ECMWF) analyses (Fig. 17). If the observed climatology is correct (and the resolved eddy transport itself is not reduced by an added drag), then any parameterized "gravity wave effects" added to the *N*90 model would only represent an arbitrary fix. In order to make more progress on this important problem, it would be desirable to pin down the magnitude of possible uncertainties in available estimates of observed atmospheric momentum transport, as well as to understand more fully the possible effects of parameterized drag on the resolved eddy transports [Boer and Lazare (1988) and Boville (1991); note that the resolved eddy momentum transports in their models are reduced by the introduction of a parameterized topographic wave drag].

The lower-stratospheric NH winter simulations in all three resolutions of the SKYHI model are reasonably good, suffering from the "cold pole" problem to only a modest degree. It is interesting that SKYHI achieves this result without the use of a subgrid-scale gravity wave drag. In fact, the present SKYHI results without gravity wave drag are similar to those obtained in Boville's (1991) spectral model with a significant parameterized topographic wave drag in the lower stratosphere. In the upper stratosphere and mesosphere the simulation of the zonal-mean state, while still reasonable, has a clear bias toward having the polar vortex too confined near the pole. The resolved eddy heat and momentum fluxes reflect this bias, with unrealistically strong fluxes being simulated at very high latitudes in the NH winter upper stratosphere and mesosphere. In this respect as well, there are striking similarities between the SKYHI simulation without gravity wave drag and those of Boville (1991) in his model with topographic gravity wave drag.

The problem with the SKYHI NH upper stratosphere may be characterized as a climatological-mean polar vortex that is unrealistically small and too nearly polar centered. It would be of interest to try to understand the sensitivity of this result to changes in both the tropospheric planetary wave structure and the upward gravity wave flux. It is certainly possible that the stratospheric vortex structure may be quite sensitive to relatively small changes in the imposed tropopause-level dynamical forcing. In particular, as the vortex is pushed farther off the pole, increased meridional excursion of air parcels can lead to a weakening of the effective radiative contraint on the flow (Fels 1985). Similarly, a weaker vortex may become more penetrable to quasi-stationary planetary waves. These issues could be attacked with appropriate three-dimensional mechanistic model studies.

The SH winter simulation is a particular problem. The lower-stratospheric temperatures and zonal winds are reasonably well represented by the model (at least in a JJA mean), although a significant cold pole bias does remain. The cold pole bias in the upper stratosphere and mesosphere is quite severe. It does improve

considerably with increasing resolution, however. This resolution dependence suggests that at least part of the model deficiency may result from an inadequate representation of the gravity wave spectrum.

Both the NH and SH summer simulation in the stratosphere and lower mesosphere appear satisfactory except for an overall cold bias, which can plausibly be attributed to the ozone climatology employed. In the upper mesosphere the model simulates a cold summer pole, but not as cold as is actually observed. This deficiency is systematically reduced with increasing model resolution, however. The negative aspect of this result is that an even higher resolution model will be required to simulate enough gravity waves to properly represent the upper-mesospheric circulation. On the other hand, it may well be that the $\sim 1°-3°$ resolution employed here is adequate to simulate a significant fraction of the gravity wave activity required to drive the circulation in the summer stratosphere and lower mesosphere.

The comparison of model results with observations attempted here has revealed both positive and negative aspects of the GCM simulation. The poor simulation of the SH winter upper stratosphere and mesosphere and the virtual lack of a QBO in the model are major problems that will require much further work. Improvement is still possible as well in many of the more favorable aspects of the present model performance. Throughout this paper differences of the order of 5°C (or sometimes more) between the model and observation have not been regarded as too worrisome. This is reasonable in light of the history and the current state of middle atmosphere comprehensive modeling. However, a much higher standard of model performance may be required before a GCM is adequate for some of the most interesting chemical applications. For example, accuracies of better than 1°C at the tropopause would be desirable for a simulation of the stratospheric water vapor field. A similar accuracy for the winter polar vortex would be needed if something like a first-principles simulation of polar stratospheric clouds (and associated heterogeneous chemistry) were to be undertaken. These considerations also reinforce the necessity to continue to improve the observational estimates of middle atmospheric climatology.

Acknowledgments. For more than a decade the late Stephen B. Fels played a crucial role in middle atmospheric modeling at GFDL. He led the development of the efficient and accurate radiation algorithms that were incorporated into SKYHI. Steve's keen insights into both radiative and dynamical aspects of middle-atmospheric circulation contributed greatly to the development of the SKYHI model. M. Daniel Schwarzkopf helped develop the radiative transfer algorithms, and he programmed the SKYHI radiation modules. He has worked very hard to implement and support the radiation code within the model. Russ Sinclair handled much of the practical coding aspect of the SKYHI model during the early years of development. Anthony J. Broccoli provided valuable advice and practical assistance with the comparison of modeled and observed precipitation fields reported in this paper. Prasad Kasibhatla found the code error in the moist convective adjustment routine. We would like to acknowledge helpful discussions with Byron Boville about the Southern Hemisphere cold pole problem, as well as other aspects of comprehensive modeling of the middle atmosphere. The authors thank A. J. Broccoli, Hiram Levy II, and Y. Hayashi for their valuable comments on the manuscript. Finally, the authors express their gratitude to the GFDL computer operations staff for their tireless efforts in running the extensive SKYHI integrations over the past decade.

APPENDIX A

Comparison of the First and Second Winters in the *N*90 Control Run

Most of the *N*90 analysis in this paper has focused on the period after the introduction of the revised radiation code and the correction of the error in the moist convective parameterization. It is illuminating to also look briefly at the *N*90 simulation before these changes were incorporated. Figure A1 shows the difference in the January mean zonally averaged temperature between *1983* and *1984*. There are a number of interesting aspects to this figure. In the troposphere the lapse rate in the first year is steeper than in the second. This is consistent with the expected effect of the code error in the convection (see section 2). The tropospheric

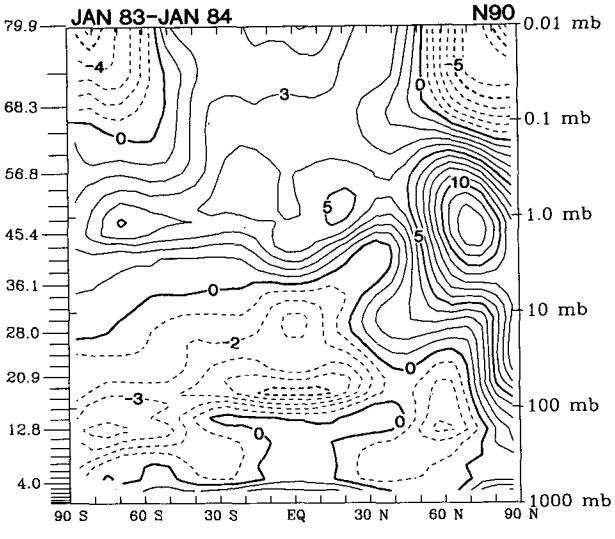

FIG. A1. The difference in the monthly mean zonally averaged temperature in the *N*90 SKYHI simulations in January *1983* and January *1984*. The contour interval is 1°C, and dashed contours indicate regions that were colder in *1983*.

changes seen in Fig. A1 are also similar to what was found when a low-resolution version of SKYHI was run with and without the code error.

In the tropical middle atmosphere the second January is warmer (colder) above (below) 10 mb than in the first January. Comparing this to the temperature bias of the second DJF period (Fig. 10), one sees that much of the tropical middle atmospheric temperature bias was introduced by the changes made in the model. The improved diurnal averaging of the solar heating rates leads to a net deeper penetration of the solar flux (and consequent reduction in heating in the upper stratosphere). The results with the new radiation code would be improved if the ozone concentrations in the upper stratosphere were increased. See the discussion in section 5.

The largest temperature differences between the two Januarys are in the high-latitude NH stratosphere. In the *N*90 run January *1983* had a very strong sudden warming (Mahlman and Umscheid 1987), while the second winter actually had no major midwinter warming. It is reasonable to suppose that the difference in the polar vortex temperatures shown in Fig. A1 primarily reflects the natural interannual variability of the model, rather than the changes in model physics (this could apply to the changes seen in the NH upper mesosphere as well, since midwinter stratospheric warmings are generally accompanied by significant cooling of the upper mesosphere). A longer integration of the *N*90 model would obviously be necessary to confirm that the model interannual variability could account for such a large difference. However, these changes are consistent with the degree of interannual variability found in the long *N*30 run; see section 5 and Hamilton (1994a, 1995).

The high-latitude summer upper mesosphere is also warmer in the second year than in the first. The natural interannual variability in the summer middle atmosphere is very small, and so this difference must be related to the alterations made in the *N*90 model. The changes in the diurnal averaging procedure are not likely to be of direct significance for the upper mesosphere (where the ozone absorption is in an optically thin range). As noted in sections 5 and 6, the summer upper mesosphere temperature is determined by a balance between radiation and the effects of gravity wave–induced mean circulations. In SKYHI a significant fraction of the gravity wave activity found in the middle atmosphere originates from convective forcing in the tropical troposphere (Manzini and Hamilton 1993). This source will obviously be affected to some extent by the correction of the error in the convection parameterization. It is likely that the ~5°C difference in the upper left corner of Fig. A1 reflects either changes in the gravity wave fluxes emerging from the troposphere and/or the effects of the changes in the tropical mean wind structure (see section 8) in filtering the gravity waves before they reach the summer mesosphere.

APPENDIX B

Simulation with Smoothed Topography

As noted in section 5, one of the major issues raised by the present control runs is the cause of the difference between the SKYHI boreal winter polar vortex and that simulated with spectral models when run without gravity wave drag. One possibly significant difference in the SKYHI model is the use of essentially unsmoothed topography versus the typical topography employed in spectral models (spectrally truncated then altered in order to reduce the sea level depressions). In order to test the effect of a smoother topography, part of the *N*30 integration was repeated with a revised topography. In order to obtain this new topographic dataset, the standard *N*30 gridded values were expanded in spherical harmonics and the resulting series was truncated to T29. This truncated harmonic representation was then evaluated on the *N*30 grid. No further alteration was applied (this meant that at some places the ocean surface points could be several hundred meters below or above the nominal sea level).

This new integration started from the initial conditions on 1 September *1985* of the *N*30 control integration. The topography was slowly deformed from the original topography to the smoothed topography over the first 15 days of September, and then the integration proceeded through the following February. The DJF mean zonally averaged zonal wind field from the end of this integration was examined (not shown). The result was notable for its similarity to the DJF climatology of the control run (Fig. 9), with the peak westerly wind about 70 m s^{-1}. It is apparent that simply smoothing the topography to something close to what might be used in a moderate-resolution spectral model does not lead to extreme changes in the simulated NH winter polar vortex.

Note added in proof. There is some recent work relevant to the comparison between the model-simulated tropical stratospheric temperatures and those in the Fleming et al. (1988) climatology (see section 5 and Figs. 10 and 12). In a wide-ranging study of various observational datasets for middle atmospheric temperature, Remsburg et al. (1994) note that the Fleming et al. values in the tropical upper (lower) stratosphere are warmer (colder) than those determined from the 7 months of *Nimbus 7* LIMS (Limb Infrared Monitor of the Stratosphere) satellite data. Thus, the present SKYHI model simulations are in better agreement with the tropical LIMS temperatures than with those of Fleming et al. Preliminary results from the *UARS* MLS remote temperatures also suggest a colder tropical upper stratosphere than indicated by Fleming et al.

REFERENCES

Andrews, D. G., J. D. Mahlman, and R. W. Sinclair, 1983: Eliassen–Palm diagnostics of wave–mean flow interaction in the GFDL

"SKYHI" general circulation model. *J. Atmos. Sci.*, **40,** 2768–2784.

Barnett, J. J., and M. Corney, 1985a: Middle atmosphere reference model derived from satellite data. *Middle Atmosphere Program Handbook,* Vol. 16, 47–85.

——, and ——, 1985b: Planetary waves. *Middle Atmosphere Program Handbook,* Vol. 16, 86–137.

Boer, G. J., and M. Lazare, 1988: Some results concerning the effect of horizontal resolution and gravity-wave drag on simulated climate. *J. Climate,* **1,** 789–806.

Boville, B. A., 1987: The validity of the geostrophic approximation in the winter stratosphere and troposphere. *J. Atmos. Sci.,* **44,** 443–457.

——, 1991: Sensitivity of the simulated climate to model resolution. *J. Climate,* **4,** 469–485.

——, and W. J. Randel, 1992: Equatorial waves in a stratospheric GCM: Effects of vertical resolution. *J. Atmos. Sci.,* **49,** 785–801.

Boyle, J. S., 1993: Sensitivity of dynamical quantities to horizontal resolution for a climate simulation using the ECMWF (Cycle 33) model. *J. Climate,* **6,** 796–815.

Broccoli, A. J., and S. Manabe, 1992: The effects of orography on midlatitude Northern Hemisphere dry climates. *J. Climate,* **5,** 1181–1201.

Cariolle, D., M. Amodei, M. Deque, J.-F. Mahfouf, P. Simon, and H. Teyssedre, 1993: A quasi-biennial oscillation signal in general circulation model simulations. *Science,* **261,** 1313–1316.

Charney, J. G., and P. G. Drazin, 1961: Propagation of planetary-scale disturbances from the lower into the upper atmosphere. *J. Geophys. Res.,* **66,** 83–109.

Cogley, A. C., and W. J. Borucki, 1976: Exponential approximation for daily average solar heating or photolysis. *J. Atmos. Sci.,* **33,** 1347–1356.

Delsol, F., K. Miyakoda, and R. H. Clarke, 1971: Parameterized processes in the surface boundary layer of an atmospheric circulation model. *Quart. J. Roy. Meteor. Soc.,* **97,** 181–208.

Emery, W. J., and K. Hamilton, 1985: Atmospheric forcing of interannual variability in the northeast Pacific Ocean, connections with El Niño. *J. Geophys. Res.,* **90,** 857–868.

Fels, S. B., 1985: Radiative–dynamical interactions in the middle atmosphere. *Advances in Geophysics,* Vol. 28A, Academic Press, 277–300.

——, J. D. Mahlman, M. D. Schwarzkopf, and R. W. Sinclair, 1980: Stratospheric sensitivity to perturbations in ozone and carbon dioxide: Radiative and dynamical responses. *J. Atmos. Sci.,* **37,** 2265–2297.

——, J. T. Kiehl, A. A. Lacis, and M. D. Schwarzkopf, 1991: Infrared cooling rate calculations in operational general circulation models: Comparisons with benchmark computations. *J. Geophys. Res.,* **96,** 9105–9120.

Fleming, E. L., S. Chandra, M. R. Schoeberl, and J. J. Barnett, 1988: Monthly mean global climatology of temperature, wind, geopotential height, and pressure for 0–120 km. NASA Tech. Memo. 100697, 85 pp.

Freidenreich, S. M., and V. Ramaswamy, 1993: Solar radiation absorption by CO_2, overlap with H_2O, and a parameterization for general circulation models. *J. Geophys. Res.,* **98,** 7255–7264.

Hamilton, K., 1982a: Stratospheric circulation statistics. NCAR Tech. Rep. TN-191+STR, 174 pp.

——, 1982b: Rocketsonde observations of the mesospheric semiannual oscillation at Kwajalein. *Atmos.–Ocean,* **20,** 281–286.

——, 1989: Evaluation of the gravity wave field in the middle atmosphere of the GFDL "SKYHI" general circulation model. WMO Tech. Doc. 273, 264–271.

——, 1993a: What we can learn from general circulation models about the spectrum of middle atmospheric motions. *Coupling Processes in the Lower and Middle Atmosphere,* E. Thrane, T. Blix, and D. Fritts, Eds., Kluwer Academic, 161–174.

——, 1993b: A general circulation model simulation of El Niño effects in the extratropical Northern Hemisphere stratosphere. *Geophys. Res. Lett.,* **20,** 1803–1806.

——, 1994a: Modelling middle atmosphere interannual variability. *Fifth COSPAR Colloq.,* M. Teague, Ed., Pergamon Press, in press.

——, 1994b: Aspects of mesospheric circulation in a comprehensive general circulation model. *The Upper Mesosphere and Lower Thermosphere, Geophys. Monogr.,* T. Killeen and R. Johnston, Eds., Amer. Geophys. Union, in press.

——, 1995: Interannual variability in the Northern Hemisphere winter middle atmosphere in control and perturbed experiments with the SKYHI general circulation model. *J. Atmos. Sci.,* **52,** 44–65.

——, and J. D. Mahlman, 1988: General circulation model simulation of the semiannual oscillation in the tropical middle atmosphere. *J. Atmos. Sci.,* **45,** 3212–3235.

——, and L. Yuan, 1992: Experiments on tropical stratospheric mean wind variations in a spectral general circulation model. *J. Atmos. Sci.,* **49,** 2464–2483.

Hayashi, Y., D. G. Golder, and J. D. Mahlman, 1984: Stratospheric and mesospheric Kelvin waves simulated in the "SKYHI" general circulation model. *J. Atmos. Sci.,* **41,** 1971–1984.

——, ——, ——, and S. Miyahara, 1989: The effect of horizontal resolution on gravity waves simulated by the GFDL SKYHI general circulation model. *Pure Appl. Geophys.,* **130,** 421–443.

Haynes, P. H., C. J. Marks, M. E. McIntyre, T. G. Shepperd, and K. P. Shine, 1991: On the "downward control" of extratropical diabatic circulations by eddy-induced mean zonal forces. *J. Atmos. Sci.,* **48,** 651–678.

Hicks, B. B., 1976: Wind profile relationships from the Wangara experiment. *Quart. J. Roy. Meteor. Soc.,* **102,** 535–551.

Hirota, I., 1978: Equatorial waves in the upper stratosphere and mesosphere in relation to the semiannual oscillation of the zonal wind. *J. Atmos. Sci.,* **35,** 714–722.

Hitchman, M., and C. B. Leovy, 1986: Evolution of the zonal mean state in the equatorial middle atmosphere during October 1978–May 1979. *J. Atmos. Sci.,* **43,** 3159–3176.

Holloway, J. L., and S. Manabe, 1971: Simulation of climate by a global general circulation model. I: Hydrological cycle and heat balance. *Mon. Wea. Rev.,* **99,** 335–370.

Holton, J. R., 1982: The role of gravity wave induced drag and diffusion in the momentum budget of the mesosphere. *J. Atmos. Sci.,* **39,** 791–799.

Hulme, M., 1991: An intercomparison of model and observed global precipitation climatologies. *Geophys. Res. Lett.,* **18,** 1715–1718.

Kantor, A. J., and A. E. Cole, 1964: Zonal and meridional winds to 120 kilometers. *J. Geophys. Res.,* **69,** 5131–5140.

Keating, G. M., and D. F. Young, 1985: Interim reference ozone models for the middle atmosphere. *Middle Atmosphere Program Handbook,* Vol. 16, 205–229.

Klinker, E., and P. D. Sardeshmukh, 1992: The diagnosis of mechanical dissipation in the atmosphere from large-scale balance requirements. *J. Atmos. Sci.,* **49,** 608–627.

Laursen, L., and E. Eliasen, 1989: On the effects of the damping mechanisms in an atmospheric general circulation model. *Tellus,* **41A,** 385–400.

Legates, D. R., and C. J. Willmott, 1990: Mean seasonal and spatial variability in guage-corrected global precipitation. *Int. J. Climatol.,* **10,** 111–127.

Levy, H., J. D. Mahlman, and W. J. Moxim, 1982: Tropospheric N_2O variability. *J. Geophys. Res.,* **87,** 3061–3080.

Lindzen, R. S., 1981: Turbulence and stress due to gravity wave breakdown. *J. Geophys. Res.,* **86,** 9707–9714.

Lubken, F. J., and U. von Zahn, 1991: Thermal structure of the mesopause region at polar latitudes. *J. Geophys. Res.,* **96,** 20 841–20 857.

McFarlane, N. A., 1987: The effect of orographically excited gravity-wave drag on the general circulation of the lower stratosphere and troposphere. *J. Atmos. Sci.,* **44,** 1775–1800.

Mahlman, J. D., and R. W. Sinclair, 1980: Recent results from the GFDL troposphere–stratosphere–mesosphere general circulation model. *Proc. ICMUA Sessions and IUGG Symp. 18,* Boulder, CO, IAMAP, 11–18.

——, and L. J. Umscheid, 1984: Dynamics of the middle atmosphere: Successes and problems of the GFDL "SKYHI" general circulation model. *Dynamics of the Middle Atmosphere,* J. R. Holton and T. Matsuno, Eds., Terra Scientific, 501–525.

——, and ——, 1987: Comprehensive modeling of the middle atmosphere: The influence of horizontal resolution. *Transport Processes in the Middle Atmosphere,* G. Visconti and R. Garcia, Eds., D. Reidel, 251–266.

——, J. P. Pinto, and L. J. Umscheid, 1994: Transport, radiative, and dynamical effects of the Antarctic ozone hole: A GFDL "SKYHI" model experiment. *J. Atmos. Sci.,* **51,** 489–508.

Manabe, S., and J. D. Mahlman, 1976: Simulation of seasonal and interhemispheric variations in the stratospheric circulation. *J. Atmos. Sci.,* **33,** 2185–2217.

——, D. G. Hahn, and J. L. Holloway, 1979: Climate simulations with GFDL spectral models of the atmosphere: Effects of spectral truncation. Report of the JOC study conference on climate models: Performance, intercomparison and sensitivity studies, Vol. 1, W. L. Gates, Ed., *GARP Publ. Ser.,* **22,** 41–94.

Manzini, E., and K. Hamilton, 1993: Middle atmospheric travelling waves forced by latent and convective heating. *J. Atmos. Sci.,* **50,** 2180–2200.

Miller, M. J., A. C. M. Beljaars, and T. N. Palmer, 1992: The sensitivity of the ECMWF model to the parameterization of evaporation from the tropical oceans. *J. Climate,* **5,** 418–434.

Miyahara, S., Y. Hayashi, and J. D. Mahlman, 1986: Interactions between gravity waves and the planetary scale flow simulated by the GFDL "SKYHI" general circulation model. *J. Atmos. Sci.,* **43,** 1844–1861.

Mlynczak, M. G., and S. Solomon, 1993: A detailed evaluation of the heating efficiency in the middle atmosphere. *J. Geophys. Res.,* **98,** 10 517–10 541.

Newell, R. E., J. W. Kidson, D. G. Vincent, and G. J. Boer, 1972: *The General Circulation of the Tropical Atmosphere and Interactions with Extratropical Latitudes.* The MIT Press, 258 pp.

Oort, A. H., 1983: *Global Atmospheric Circulation Statistics.* NOAA Prof. Paper No. 14, 180 pp.

Palmer, T. N., G. J. Shutts, and R. Swinbank, 1986: Alleviation of a systematic westerly bias in general circulation and numerical weather prediction models through an orographic gravity wave parameterization. *Quart. J. Roy. Meteor. Soc.,* **112,** 1001–1039.

Paolo, S. E., and S. K. Avery, 1993: Mean winds and the semiannual oscillation in the mesosphere and lower thermosphere at Christmas Island. *J. Geophys. Res.,* **98,** 20 385–20 400.

Peltier, W. R., and T. L. Clark, 1979: The evolution and stability of finite-amplitude mountain waves. Part II: Surface drag and severe downslope windstorms. *J. Atmos. Sci.,* **36,** 1498–1529.

Randel, W. J., 1992: Global atmospheric circulation statistics, 1000–1 mb. NCAR Tech. Note TN-366+STR, 256 pp.

Reed, R. J., 1965: The quasi-biennial oscillation of the atmosphere over Ascension Island. *J. Atmos. Sci.,* **22,** 331–333.

Remsburg, E. E., P. P. Bhatt, and T. Miles, 1994: An assessment of satellite temperature distributions used to derive the net diabatic transport for zonally averaged models of the middle atmosphere. *J. Geophys. Res.,* in press.

Rind, D., R. Suozzo, N. K. Balachandran, A. Lacis, and G. Russell, 1988a: The GISS global climate–middle atmosphere model. Part I: Model structure and climatology. *J. Atmos. Sci.,* **45,** 329–370.

——, ——, and N. K. Balachandran, 1988b: The GISS global climate–middle atmosphere model. Part II: Model variability due to interactions between planetary waves, the mean circulation, and gravity wave drag. *J. Atmos. Sci.,* **45,** 371–386.

Rosenfeld, J. E., M. R. Schoeberl, and M. A. Geller, 1987: A computation of the stratospheric diabatic circulation using an accurate radiative transfer model. *J. Atmos. Sci.,* **44,** 859–876.

Sassi, F., R. R. Garcia, and B. A. Boville, 1993: The stratopause semiannual oscillation in the NCAR Community Climate Model. *J. Atmos. Sci.,* **50,** 3608–3624.

Schubert, S., S. Moorthi, C.-K. Park, M. Suarez, and W. Higgins, 1990a: An atlas of ECMWF analyses—Part I. NASA Tech. Memo. 100747.

——, ——, W. Higgins, M. Suarez, and C.-K. Park, 1990b: An atlas of ECMWF analyses—Part II. NASA Tech. Memo. 100762.

Schwarzkopf, M. D., and S. B. Fels, 1985: Improvements to the algorithm for computing CO_2 transmissivities and cooling rates. *J. Geophys. Res.,* **90,** 10 541–10 550.

Shine, K., 1989: Sources and sinks of zonal momentum in the middle atmosphere using the diabatic circulation. *Quart. J. Roy. Meteor. Soc.,* **115,** 265–292.

Strahan, S. E., and J. D. Mahlman, 1994a: Evaluation of the GFDL "SKYHI" general circulation model using aircraft N_2O measurements: 1. Polar winter stratospheric meteorology and tracer morphology. *J. Geophys. Res.,* **99,** 10 305–10 318.

——, and ——, 1994b: Evaluation of the GFDL "SKYHI" general circulation model using aircraft N_2O measurements: 2. Tracer variability and diabatic meridional circulation. *J. Geophys. Res.,* **99,** 10 319–10 332.

van Loon, H., R. L. Jenne, and K. Labitzke, 1973: Zonal harmonic standing waves. *J. Geophys. Res.,* **78,** 4463–4471.

Wallace, J. M., S. Tibaldi, and A. J. Simmons, 1983: Reduction of systematic errors in the ECMWF model through the introduction of envelope topography. *Quart. J. Roy. Meteor. Soc.,* **109,** 683–717.

Wang, W.-C., M. P. Dudek, X.-Z. Liang, and J. T. Kiehl, 1991: Inadequacy of effective CO_2 as a proxy in simulating the greenhouse effect of other radiatively active gases. *Nature,* **350,** 573–577.

Wu, M. F., M. A. Geller, E. R. Nash, and M. E. Gelman, 1987: Global atmospheric circulation statistics—Four year averages. NASA Tech. Memo. 100690, 70 pp.

Zwiers, F., 1993: Simulation of the Asian summer monsoon with the CCC GCM-1. *J. Climate,* **6,** 470–486.